SYNTHESIS OF CABON NANO TUBES AND OTHER NANOSTRUCTURES AND THEIR FIELD EMISSION STUDIES

A dissertation Submitted in Partial Fulfilment of the

Requirements for the Award Degree of

Master of Technology

in

Materials Science and Engineering

By

Vishakha Kaushik

Roll No. 60702020

Under the Supervision of

Prof. V.D. Vankar

Department of Physics

IIT Delhi

Prof. K. K. Raina

Department of SPMS

Thapar University, Patiala

School of Physics and Materials Science

THAPAR UNIVERSITY,

PATIALA-147004, June- 2009

CERTIFICATE

This is to certify that the project entitled ***"Synthesis of Carbon Nanotubes and other nanostructures and their field emission Studies"****, presented by* ***Vishakha Kaushik*** *roll no.* ***60702020*** *and* ***2008VST0086*** *(in IIT Delhi), is worthy of consideration for the award of the degree of* ***Master of Technology*** *in* ***Materials Science and Engineering*** *and is a record of the original bona fide research work carried out by her under our supervision and that the results contained in it have not been submitted in part or full, to any other university or institute for the award of any degree or diploma.*

8.6.09

Prof. K. K. Raina

Dean of Faculty Affairs

&

Dean of Resource Planning and Generation

Department of SPMS, Thapar University,

Patiala- 147004, Panjab,

Prof. V. D. Vankar,

Department of Physics,

Indian Institute of Technology Delhi,

Hauz Khas, New Delhi-110016

INDIA.

CERTIFICATE

This is to certify that the project entitled ***"Synthesis of Carbon Nanotubes and other nanostructures and their field emission Studies"****, presented by* ***Vishakha Kaushik*** *roll no.* ***60702020*** *and* ***2008VST0086*** *(in IIT Delhi), is worthy of consideration for the award of the degree of* ***Master of Technology*** *in* ***Materials Science and Engineering*** *and is a record of the original bona fide research work carried out by her under our supervision and that the results contained in it have not been submitted in part or full, to any other university or institute for the award of any degree or diploma.*

Prof. K. K. Raina

Dean of Faculty Affairs

&

Dean of Resource Planning and Generation

Countersigned

Dr. O.P. Pandey

(Prof. & Head)

SPMS, Thapar University, Patiala

Dr. R. K. Sharma

Dean, Academic Affairs

Thapar University, Patiala

ACKNOWLEDGEMENT

With full of honour and respect, I express my deep sense of gratitude and indebtedness to ***Prof. V. D. Vankar, Physics department, IIT Delhi*** for his co-operation, inspiring guidance and constant help at all stages of my project work. His constant encouragement and concern during the execution of the present work would be remembered with gratefulness for all times to come.

I would like to express my gratitude to ***Prof. K.K. Raina, SPMS, Thapar University, Patiala,*** for his patient guidance and support throughout the project. It was both an honour and a privilege to work with him. He also provided genuine help in developing technical writing and presentation skill and I found this guidance to be extremely valuable.

With special concern, I express my honest gratitude to ***Mr. Sandeep Chhoker***, for his constant support during the entire project work. Despite of quite business, he helped me whenever I was in need. His valuable suggestions helped me very much in overcoming various difficulties at many stages of my work. His help and care never let me feel disheartened. The open discussion with him helped me to think beyond the literature and encouraged to find out various possibilities to sort out the technical problems.

With immense pleasure I wish to express my sincere thanks to ***Mrs. Sangeeta Handuja*** for her worthwhile suggestions and constant inspiration during all stages of my project work. Her special qualities including her dedication made me to learn much more beyond getting a technical bent of mind.

I am really thankful to ***Mrs. Himani Sharma*** to be always companion and genuinely supportive. Frank discussions with her many times helped me overcome the difficulties.

I convey my sincere thanks to ***Dr. Deepak Varandani*** and ***Ms. Rupali Nagar*** for their kind help and suggestions at various stages of my project work.

The most importantly; it is a great pleasure to thank my M. Tech. friends ***Pragya Agar***, ***Anjali Yadav, Monika Sharma, Pooja Girdhar***, ***Geetanjali Kalra***, ***and Swarnakamal Priyabadini*** for their moral support. Their good humoured company made my stay in IIT

Delhi pleasant and memorable. They mean more than friends for me. The bond of love with them will be kept as treasure, for all times to come.

I am also thankful to all of my friends who devoted their valuable time and helped me in all possible ways towards successful completion of this work. The words would be less to express the thanks to all the members of Thin Film Laboratory, for their help, inspiration and moral support which went a long way in successful completion of my work. I thank all those who have contributed directly or indirectly to this work.

Lastly, and more importantly, I would like to thank my parents for their years of unyielding love and encouragement. They always wished the best for me and I acknowledge my parents' determination and sacrifice to put me through the higher studies.

VISHAKHA KAUSHIK Date: 08/06/09

Abstract

Discovered in 1991, carbon nanotubes (CNTs) have reached the forefront of many industrial research projects. Carbon nanotubes are tubular graphene layers with remarkable mechanical, chemical, thermal and electrical properties, which make them useful in various applications. Depending upon their structure CNTs are of two types i.e. single walled carbon nanotube (SWCNT) and multiwalled carbon nanotube (MWCNT).

The nucleation and growth of vertically aligned MWCNT deposited on p-Si substrate by microwave plasma enhanced chemical vapour deposition (MPECVD) process have been carried out. Several characterization techniques such as: scanning electron microscopy, transmission electron microscopy, high resolution transmission electron microscopy, energy dispersive spectroscopy, Raman spectroscopy and glancing angle X-ray diffraction were used for characterization of carbon nanostructures.

Various parameters were found to affect the growth and microstructures of nanostructured carbon films like: gas flow ratio, deposition time and cocatalyst thickness. Carbon nanowalls were deposited using Ag-Fe coated Si substrates. Continuous decrease in density and increase in size of carbon nanowalls with increase in growth time was observed.

Field emission characteristics of different CNTs and CNWs carried out using a diode configured field emission system. The threshold field and field enhancement factor were determined from the current density vs. electric field and Fowler-Nordheim plots for different samples. It was found that Ag-Fe deposited films have better emission properties as compared to CNT film deposited on Fe. CNWs also have good emission characteristics. CNWs deposited for higher time were found as better emitters.

Table of Contents

CHAPTER 2: Experimental and Characterization Techniques

CHAPTER 3: Growth and Characterization of Carbon Nanostructures

List of Figures

CHAPTER 1: Introduction

CHAPTER 2: Experimental and Characterization Techniques

CHAPTER 3: Growth and Characterization of Carbon Nanostructures

CHAPTER 4: Field Emission Properties of Carbon nanostructures

List of Tables

CHAPTER 1: Introduction

CHAPTER 3: Growth and Characterization of Carbon Nanostructures

CHAPTER 4: Field Emission Properties of Carbon nanostructures

CHAPTER 1

Introduction

This chapter introduces the field of carbon nanostructures like CNT, CNF, CNP, CNW etc. Various properties of CNT have been discussed. The synthesis techniques of carbon nanostructures and various proposed growth mechanisms have been described. Application of carbon nanotubes has been discussed.

1.1 Carbon Nanotubes (CNTs)

Carbon, a group IV element, has two crystalline forms: diamond and graphite. Carbon nanotubes (CNTs) are allotropes of carbon. These cylindrical carbon molecules have novel properties that make them potentially useful in many applications in nanotechnology, electronics, optics and other fields of materials science, as well as potential uses in architectural fields. They exhibit extraordinary strength and unique electrical properties, and are efficient conductors of heat. CNTs are members of the fullerene structural family, which also includes the spherical buckyballs [1]. The ends of a CNT might be capped with a hemisphere of the buckyball structure. CNTs are named on the basis of derived from their size, since the diameter of a nanotube is on the order of a few nanometers, while they can be up to several millimetres in length[2]. CNTs are categorized as single-walled nanotubes (SWCNTs) and multi-walled nanotubes (MWCNTs) depending upon the number of walls.

CNTs may consist of one up to tens and hundreds of concentric shells of carbons with adjacent shells separation of ~0.34 nm i.e. (002). The carbon network of the shells is closely related to the honeycomb arrangement of the carbon atoms in the graphite sheets. The amazing mechanical and electronic properties of the nanotubes stem in their quasi-one-dimensional (1D) structure and the graphite-like arrangement of the carbon atoms in the shells. Thus, the nanotubes have high Young's modulus and tensile strength, which makes them suitable for composite materials with improved mechanical properties. The nanotubes can be metallic or semiconducting depending on their structural parameters. This opens the way for application of the nanotubes as central elements in electronic devices[3] including

field-effect transistors[4] (FET), single-electron transistors and rectifying diodes. Possibilities for using of the nanotubes as high-capacity hydrogen storage media have also been considered[5].

1.2 Structure of Carbon Nanotubes[6]

It is convenient to specify a general CNT in terms of a vector C_h , and the chiral angle θ, which are shown in Fig.1.1. The chiral vector C_h is defined in Table1.1 in terms of the integers (n,m) and the basis vectors a and b of the graphene sheet, which are also given in the table in terms of rectangular coordinates. The integers (n,m) uniquely determine C_h and θ. The length L of the chiral vector C_h (Table1.1) is directly related to the tubule diameter d. The chiral angle θ between the C_h direction and the zigzag direction of the graphene sheet (n,0) (Fig.1.1) is related in Table 1.1 to the integers (n, m). We can specify a single-wall carbon nanotube by rolling of graphene[7] sheet that the two end points of C_h superimposed to one another.

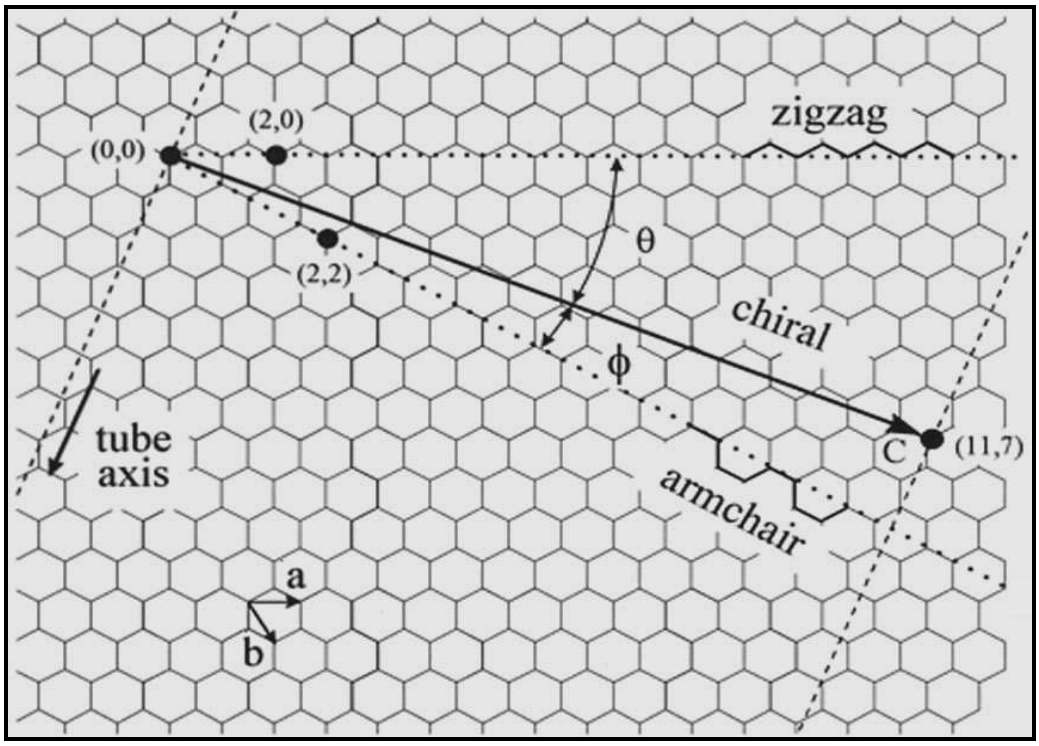

Fig.1.1: Graphene sheet with the lattice vectors a and b and angle θ and φ show the type of nanotube : Armchair, Zigzag, Chiral[41].

Table 1.1 Different parameters of carbon nanotubes (CNTs).

Name	Formula	Value
Carbon-Carbon distance	C-C	1.421 Aº
Length of unit vector	$\sqrt{3}a_{c\text{-}c}$	2.46Aº
Chiral vectors	$\vec{C_h} = \vec{na} + \vec{mb}$	n,m integers
Circumference of nanotubes	$L=C_h=a\sqrt{(n^2+m^2+nm)}$	0<m<n
Circumference of nanotubes	$d_t = \frac{a\sqrt{(n^2+m^2+nm)}}{\pi}$	.....
Chiral angle	$\sin\theta = \frac{\sqrt{3}m}{2\sqrt{(n^2+m^2+nm)}}$	.....

The unit cell of the carbon nanotube is shown in Fig.1.1 as the rectangle bounded by the vectors C_h and tube axis.

There are two types of CNT: Single walled carbon nanotubes (SWCNT) and Multiwalled carbon nanotubes (MWCNT). A SWCNT is a hollow cylinder of a graphite sheet. The inner diameter of SWNT is typically 1 nm. MWCNT consists of many concentric seamless cylinders or SWNTs. The intertube spacing in MWNTs is typically ~ 0.34 nm. The diameter of MWNTs ranges from 2 nm to 25 nm as shown in fig 1.2.

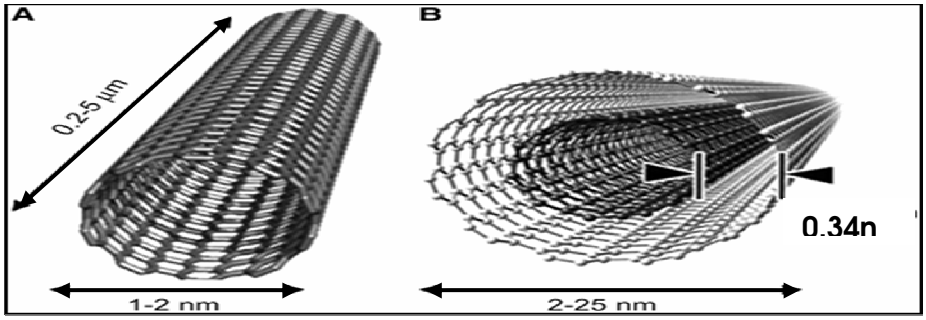

Fig.1.2: Schematic diagram of (A) Singlewalled CNT (B) Multiwalled CNT[42].

Depending on the orientation of vector C, nanotubes are classified into three categories:

(a) **Armchair tubes**, for this, n = m, i.e. all (n,n) tubes are called armchair tubes.

(b) **Zigzag tubes**, for this, m = 0, i.e. all (n,0) tubes are called zigzag tubes.

(c) All other tubes are called chiral tubes with a chiral angle, θ, defined as angle between the vector C and the zigzag direction as shown in fig 1.3.

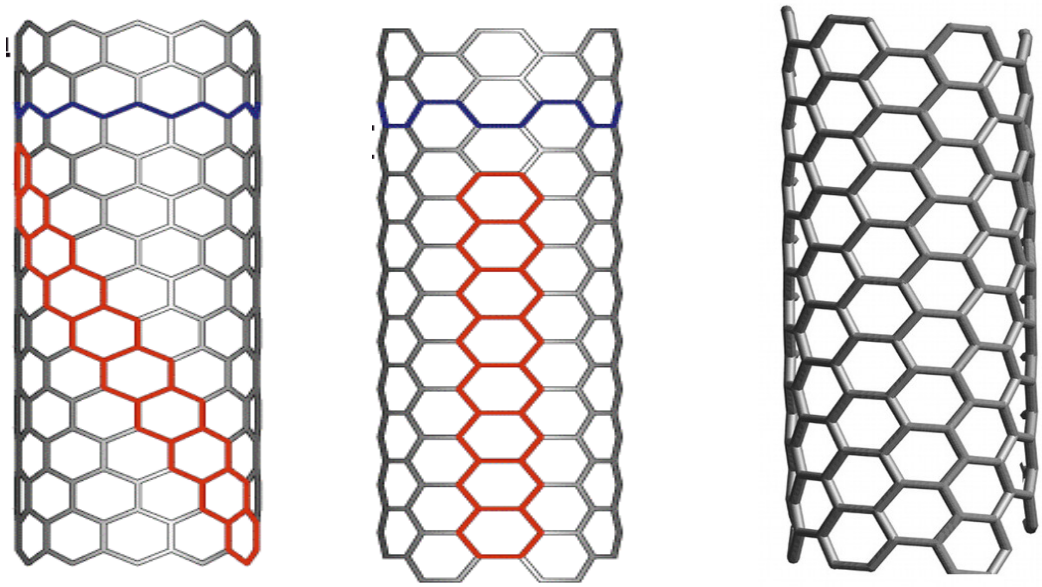

(a) **(b)** **(c)**

Fig: 1.3 Schematic models of (a) zigzag (b) Armchair and(c) Chiral CNT[42].

1.3 Properties of CNT

CNT is a arrangement of carbon atoms that possess unique set of specific properties: mechanical, electrophysical, field-emission, optical and chemical. Utilization of CNTs filled by nanoparticles of different materials comes as a significant step forward in the development of nanotechnology. The investigation of the properties of CNT coupled with the magnetic materials is one of the most advanced area of research. They have variable electronic and mechanical properties. They can carry the highest current density among any material. They have high aspect ratio and high melting point.

1.3.1 Electronic Properties

Electronic properties of CNT have received the greatest attention in nanotube research and applications. Extremely small size and the highly symmetric structure account for the

remarkable electronic and magnetic properties of the nanotubes. SWCNTs, ropes of SWCNTs and MWCNTs show quantum wire characteristics. MWCNTs are essentially non semiconducting[8] or metallic, whereas, SWCNTs can be either metallic or semiconducting (band gap ~ 0.4 - 0.9) depending on their precise structure. SWCNTs possess special properties which emerge from the strong one dimensionality and crystalline perfection of the cylindrical graphene structure. The band gap for a semiconducting tube ($n - m \neq 3k$) is given by

$$E_g = 2\, d_{cc}\, \gamma / D$$

where γ is the nearest neighbour – hopping parameter and ranges between 2.5-3.2 eV, d_{cc} = 0.142 nm, C-C bond length and D is the tube diameter[9].

1.3.2 Electrical Properties

In view of the symmetry and unique electronic structure of graphene, the structure of a CNT strongly affects its electrical properties. CNT exhibits very high electrical conductivity along its axis. For a given (n,m) nanotube, if n = m, the CNT is metallic; if n − m is a multiple of 3, then the nanotube is semiconducting with a very small band gap, otherwise the CNT is a moderate semiconductor. Thus all (n=m) CNT are metallic, and CNT (5,0), (6,4), (9,1), etc. are semiconducting. In theory, metallic CNT can carry an electrical current density of 4×10^9 A/cm^2 which is more than 1,000 times greater than metals, such as, copper[10].

1.3.3 Thermal Properties[11]

All CNT are expected to be excellent thermal conductors along the tube, exhibiting a property known as “ballistic conduction” but good insulators laterally to the tube axis. Because of their small size, quantum effects are important, and the low-temperature specific heat and thermal conductivity show direct evidence of 1D quantization of the phonon bandstructure. It is predicted that CNT would be able to transmit up to 6000 W/m.K at room temperature while copper transmits 385 W/m.K. The temperature stability of CNT is estimated to be up to 2800^0C in vaccum and about 750^0C in air. At higher temperature, a SWCNT,SWCNT bundle, and MWCNT all have specific heat values close to graphite.

However, at lower temperature, because of quantum confinement effects they show unusual behavior.

1.3.4 Mechanical Properties

CNT have high strength, coupled with extraordinary flexibility and resilience. The small diameter of a carbon nanotube also has an important effect on the mechanical properties, compared with traditional micron-size graphitic fibres. Perhaps the most striking effect is the opportunity to associate high flexibility and high strength with high stiffness[12,13], a property that is absent in graphite fibres. These properties of CNTs open the way for a new generation of high performance composites[5,10]. The mechanical properties are strongly dependent on the structure of the CNT. Some of the properties are as shown in table 1.2.

Table 1.2 Mechanical properties of carbon nanotubes.

	Young's modulus (TPa)	**Tensile Strength (GPa)**	**Density (g/cm^3)**
MWNT	1.20	150	2.6
SWNT	1.054	75	1.3
Graphite	0.35	75	2.6

1.4 Applications of CNTs

CNTs have extraordinary electrical conductivity, heat conductivity and mechanical properties. They are probably the best electron field-emitter. They are polymers of pure carbon and can be reacted and manipulated using the tremendously rich chemistry of carbon. This provides opportunity to modify the structure and to optimise solubility and dispersion.

Furthermore, CNTs are molecularly perfect, which means that they are free of property-degrading flaws in the nanotube structure. Their material properties can therefore approach closely the very high levels intrinsic to them. These extraordinary characteristics give buckytubes potential in numerous applications.

1.4.1 Field Emission

CNT are the best known field emitters of any material due to the sharpness of their tip[14]. The sharper the tip, the more concentrated will be an electric field, leading to better field emission. The sharpness of the tip also means that they emit at especially low voltage, an important fact for building electrical devices that utilize this feature. CNT can carry high current density, possibly as high as 1013 A/cm^2. Furthermore, the current is extremely stable[15].

An immediate application of this behaviour receiving considerable interest is in field-emission flat-panel displays. Instead of a single electron gun, as in a traditional cathode ray tube display, there is a separate electron gun (or many) for each pixel in the display. The high current density, low turn-on and operating voltage, and steady, long-lived behaviour make buckytubes attract field emitters to enable this application. Other applications utilising the field-emission characteristics of CNT include: cold-cathode lighting sources, lightning arrestors, and electron microscope sources[16].

1.4.2 Energy Storage

CNT have the intrinsic characteristics desired in material used as electrodes in batteries and capacitors, two technologies of rapidly increasing importance. Buckytubes have a tremendously high surface area (~1000 m^2/g), good electrical conductivity, and very importantly, their linear geometry makes their surface highly accessible to the electrolyte.

Research has shown that CNTs have highest reversible capacity of any carbon material for use in lithium-ion batteries[17]. In addition, CNTs are outstanding materials for supercapacitor electrodes[18] and are now being marketed. CNTs also have applications in a variety of fuel cell components. They may also be used in gas diffusion layers as well as current collectors because of their high electrical conductivity. Their high strength and toughness to weight characteristics may also prove valuable as part of composite components in fuel cells that are deployed in transport applications where durability is extremely important.

1.4.3 Conductive Adhesives and Connector

The CNTs are attractive as conductive fillers for use in shielding, and electronics materials, such as, adhesives and other connectors (e.g., solders).

1.4.4 Molecular Electronics

The idea of building electronic circuits out of the essential building blocks of materials - molecules - has seen a revival in the past five years, and is a key component of nanotechnology. In any electronic circuit, but particularly as dimensions shrink to the nanoscale, the interconnections between switches and other active devices become increasingly important.Their geometry, electrical conductivity, and ability to be precisely derived, make CNT the ideal candidates for the connections in molecular electronics. In addition, they have been demonstrated as switches themselves.

1.4.5 Thermal Materials

The record-setting anisotropic thermal conductivity of CNT is enabling applications where heat needs to move from one place to another. Such an application is electronics, particularly advanced computing, where uncooled chips now routinely reach over 100^{o}C.

CNI's technology for creating aligned structures and ribbons of CNT[19] is a step toward realising incredibly efficient heat conduits. In addition, composites with CNT have been shown to dramatically increase the bulk thermal conductivity at small loadings.

1.4.6 Solar Cells

Solar cells developed at the New Jersey Institute of Technology use a carbon nanotube complex, formed by a mixture of CNT and buckyballs (known as fullerenes) to form snake-like structures. Buckyballs trap electrons, although they can't make electrons flow. Add sunlight to excite the polymers, and the buckyballs will grab the electrons. Nanotubes, behaving like copper wires, will then be able to make the electrons or current flow.

1.5 Synthesis of CNTs

There are three techniques for the growth of MWCNTs:

1. Arc discharge
2. Laser ablation
3. Chemical vapour deposition (CVD)

1.5.1 Arc discharge

The arc-discharge method is the one by which CNTs were first produced and recognized. In arc discharge method, two graphite rods are used. Firstly the chamber is evacuated with a vacuum pump, and then an appropriate ambient gas is introduced at the desired pressure. Thereafter a dc arc voltage[20] is applied between the two graphite rods (Fig 1.4). When pure graphite rods are used, the anode evaporates to form fullerenes [21], which are deposited in the form of soot in the chamber. However, a small part of the evaporated anode is deposited on the cathode, which includes CNTs. These CNTs, made of coaxial graphene sheets and called MWNTs, are found not only on the top surface of the cathode deposit[22] but also deep inside the deposit[20].

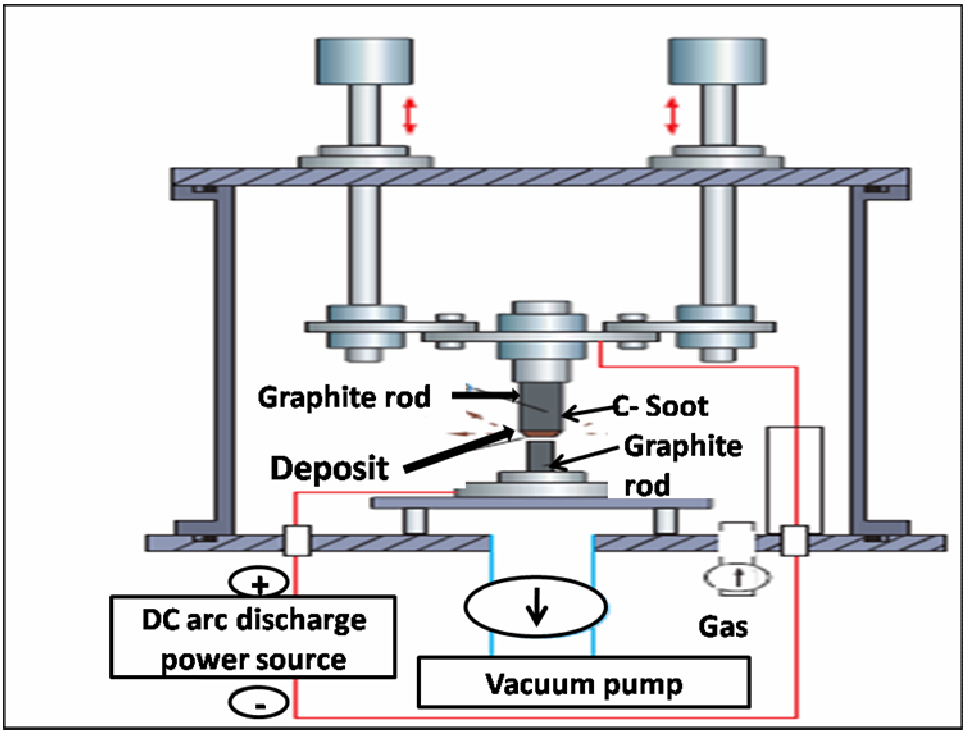

Fig: 1.4 Schematic diagram of Arc discharge method[44].

Large-scale synthesis of MWNTs by arc discharge has been achieved[23,24] using He gas. When a graphite rod containing metal catalyst (Fe, Co, etc.) is used as the anode with a pure graphite cathode, single-walled carbon nanotubes (SWNTs) [25,26] are generated in the form of soot. It was found that CH_4 gas was the best for forming MWNTs with high crystallinity with few coexisting carbon nanoparticles. The hydrogen arc discharge is used to producing MWNTs with high crystallinity[27], and a new morphology of carbon, the 'carbon rose[28].

1.5.2 Laser Ablation

Historically, laser ablation was the first technique used to generate fullerene clusters in the gas phase[29]. Carbon is vaporized from the surface of a solid disk of graphite into a high-density helium (or argon) flow, using a focused pulsed laser[30,31]. A graphite target is placed in the middle of a long quartz tube mounted in a temperature controlled furnace (Fig.1.5).

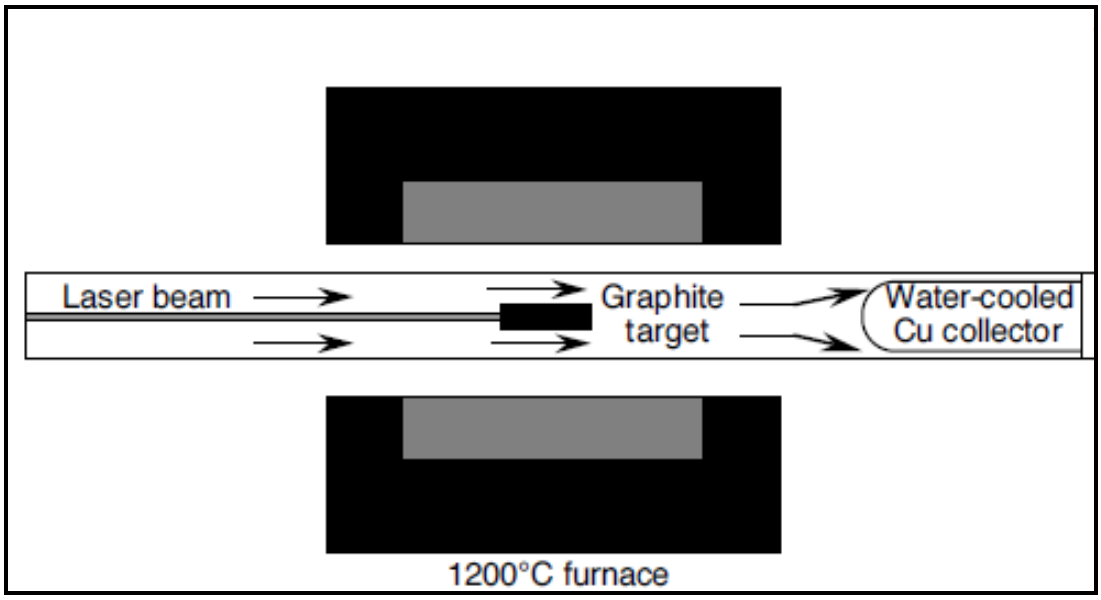

Fig : 1.5 Schematic diagram of laser ablation[45].

After the sealed tube has been evacuated, the furnace temperature is increased to 1200^{o}C. The tube is then filled with a flowing inert gas and a scanning laser beam is focused onto the graphite target by way of a circular lens. The laser vaporization produces carbon species, which are swept by the flowing gas from the high-temperature zone and deposited on a conical water-cooled copper collector.

These nanotubes are formed with 4 to 24 graphitic layers and their lengths can reach 300 nm. Their yield and quality are dependent on the furnace temperature. At 1200^{o}C all the observed nanotubes are free of defects and closed at the end. If the oven temperature is decreased to 900^{o}C the number of defects increases, and below 200^{o}C no nanotubes are found[32]. When a small amount of transition metal has been added to the carbon target, SWNTs are produced. However, during this process, the surface of the target becomes metal-rich and the yield of SWNTs decreases.

1.5.3 Chemical Vapour Deposition (CVD)

CVD is a common method for the commercial production of carbon nanotubes. CVD is a process of chemically reacting a volatile compound of a material to be deposited, with other gases, to produce a non-volatile solid that deposits atomistically on a suitably placed substrate. Today, high temperature CVD process for producing thin films and coatings have found increasing applications in such diverse technologies as the fabrication of solid-state electronic devices, the manufacture of ball bearings and cutting tools, and the production of rocket engine and nuclear reactor components[33].

The fundamental sequential steps that occur in every CVD process are shown in fig.1.4 and include:

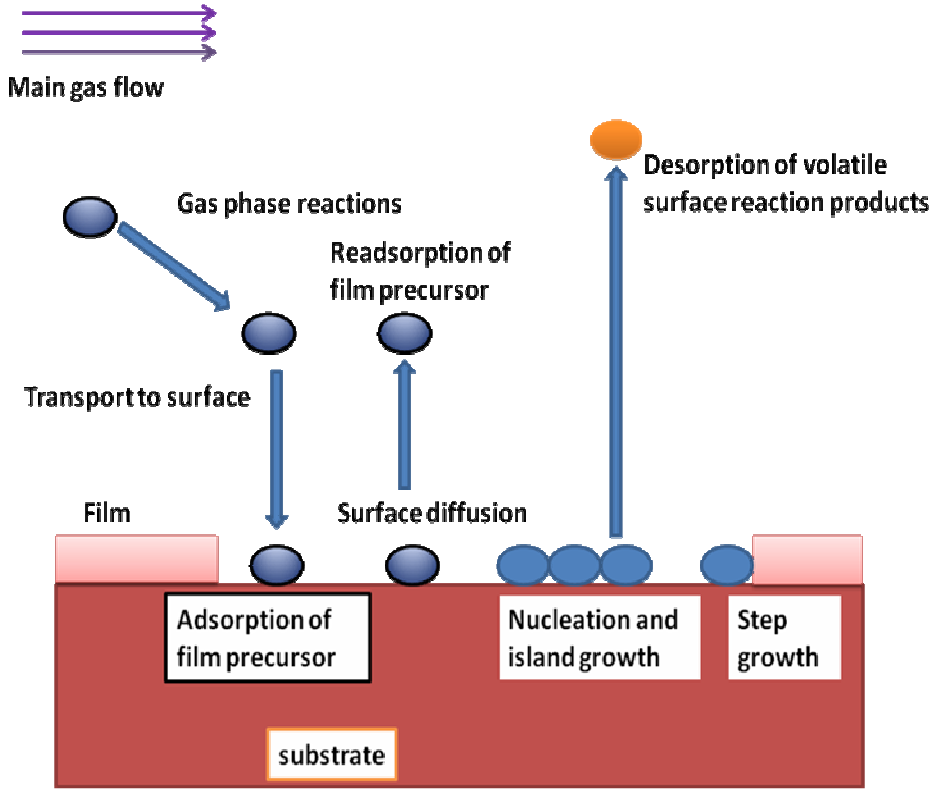

Fig. 1.6: Sequence of gas transport and reaction process contributing to CVD film growth[33].

1. Convective and diffusive transport of reactans from the gas inlets to the reaction zone.
2. Chemical reactions in the gas phase to produce new reactive species and by products.
3. Transport of the initial reactants and their products to the substrate surface.
4. Adorbtion (chemical and physical) and diffusion of these species on the substrate surface.
5. Heterogeneous reactions catalyzed by the surface leading to film formation.
6. Desorption of the volatile by products of surface reactions.
7. Convective and diffusive transport of the reaction by products away from the reaction zone.

1.5.3.1 Thermal CVD

In this method Fe, Ni, Co or an alloy of the three catalytic metals is initially deposited on a substrate. The specimen is placed in a quartz boat. The boat is positioned in a CVD reaction furnace, and nanometre-sized catalytic metal particles are formed after an additional etching of the catalytic metal film using NH_3 gas at a temperature of 750 to 1050 ^oC. For growing carbon nanotubes some hydrocarbon, such as, methane, ethane, acetylene, ethylene is used as carbon source. Figure 1.6 shows a schematic diagram of thermal CVD apparatus in the synthesis of carbon nanotubes. The nanotubes formed are MWCNTs[34].

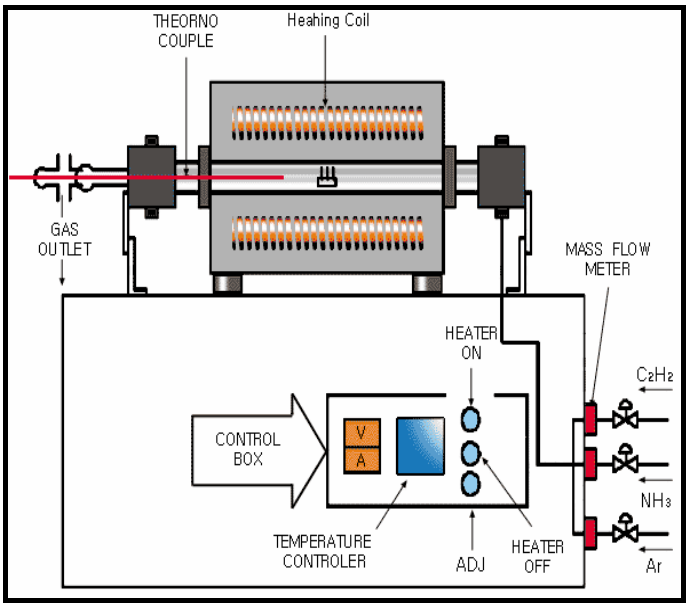

Fig.1.7: Schematic diagram of thermal CVD apparatus[46].

1.5.3.2 Plasma enhanced chemical vapour deposition (PECVD)

The plasma enhanced CVD method generates a glow discharge in a chamber or a reaction furnace by a high frequency voltage applied between two electrodes. Figure 1.7 shows a schematic diagram of a typical plasma CVD apparatus with a parallel plate electrode structure. The substrate is placed on the grounded electrode. In order to form a uniform film, the reaction gas is supplied from the opposite plate. Catalytic metal, such as, Fe, Ni and Co are used on for example a Si, SiO_2, or glass substrate using thermal CVD or sputtering. After nanoscopic fine metal particles are formed, a carbon containing reaction gas, such as C_2H_2, CH_4, C_2H_4, C_2H_6, CO is supplied to the chamber during the discharge[35]. Carbon nanotubes will be grown over the metal particles on the substrate by glow discharge generated from high frequency power.

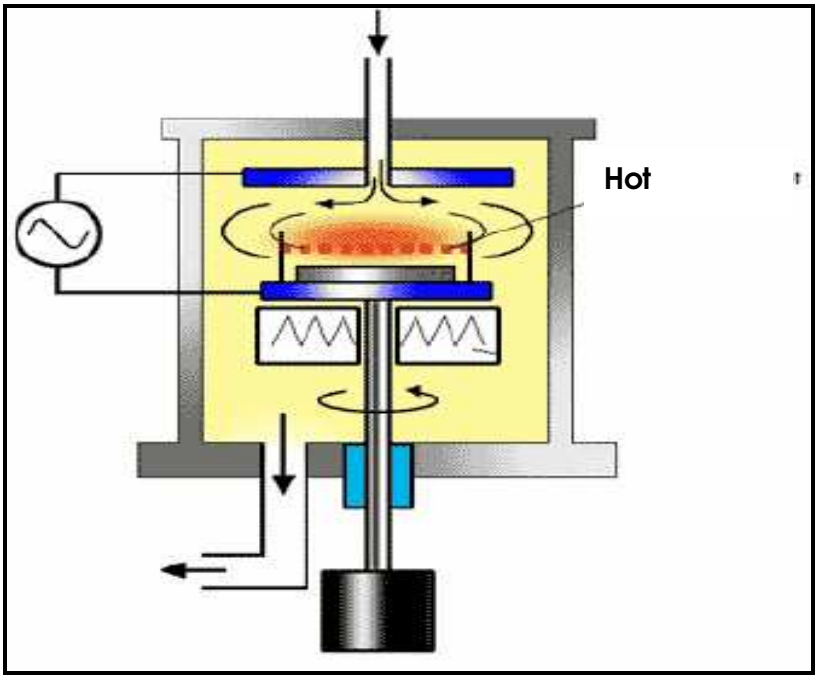

Fig.1.8: Schematic diagram of plasma CVD apparatus[46].

The catalyst has a strong effect on the nanotube diameter, growth rate, wall thickness, morphology and microstructure. Ni seems to be the most suitable pure-metal catalyst for the growth of aligned multiwalled carbon nanotubes (MWNTs). The diameter of the MWNTs is approximately 15 nm. The highest yield of carbon nanotubes was about 50% achieved at relatively low temperatures (below 330^{o}C). There are various types of PECVD process as follows:

(a) DC plasma enhanced CVD

(b) Plasma assisted hot filament CVD

(c) RF –plasma enhanced CVD

(d) Microwave plasma Enhanced CVD

In our experiment we have used **microwave plasma enhanced CVD**. Microwave plasma is different from other plasma sources. In this method power coupling to the plasma is achieved from microwave source and electrode holding the substrate can be independently biased with a DC or RF source at the desirable levels. It exhibits several properties and offers the unique characteristics of the microwave plasma, as discussed below: It can be maintained at high gas pressures, the electron density is higher in the microwave plasma than others and its reactivity is expected to be very high [36]. The high electron temperature (1-10eV) and high plasma density ($10^{11}/cm^2$) result in high density of nucleation and growth rate. It is an electrodeless discharge, thus provides contamination free deposition of CNTs.

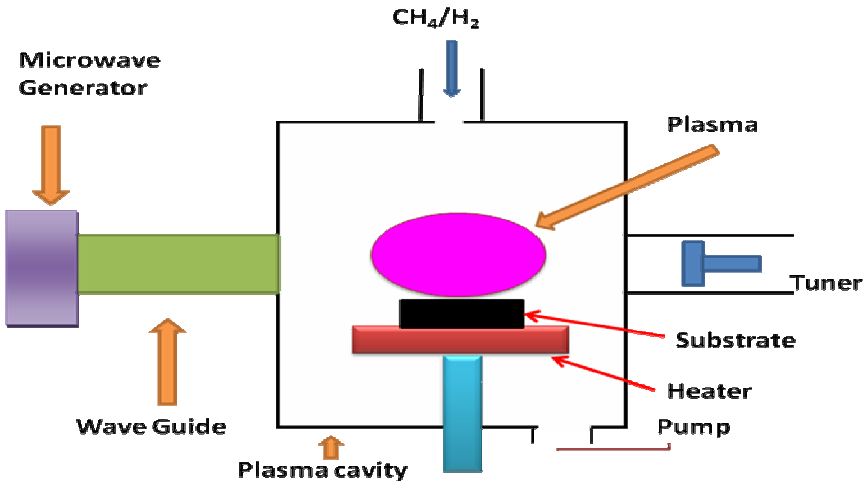

Fig.1.9: Schematic diagram of Microwave plasma enhanced CVD[37].

Microwave plasma enhanced CVD (MPECVD) is very popular high frequecy plasma CVD technique[37,38] as shown in fig 1.9. MPECVD consists of a 2.45GHz microwave generator and power coupling is achived through rectangular wave guide. The reacton chamber is a quarz tube, placed in the path of the micorwaves through an applicator in the

rectangular wave guide. The substrate is loaded in the reactor on an electrically floating substrate holder. Plasma of hydrocarbon-diluent mixture is sustained in the reactor at desired power level and discharge pressures and carbon films are deposited on the substrate. The substate is heated by both the highly energetic plasma species and the microwave radiation. In this method the large area deposition of CNTs is not possible due to the confined plasma within the quartz tube forming the cavity and the size of the tube is limited by the wave guide dimensions. The resulting film may be contaminated as a result of etching of the quartz tube by the atomic hydrogen and energetic ions produced in the plasma, if very high power is used.

1.6 Growth Mechanism of CNTs

In general two possible mechanisms have been proposed for the growth of CNT as described below.

(a) Base growth mechanism

When there is a strong interaction between the metal and support, then this mechanism is assumed to be adopted for the growth of CNT. If there exists a strong interaction between the metal and support the hydrocarbon molecule which is used as the source of the carbon for the growth of carbon nanotubes cannot lift the metal particle from the support[39]. Then the tube grows away from the metal particle which is deposited on the surface of the support. Here the metal particle helps only in the nucleation of the CNT. Fig 1.10 shows the base growth mechanism of CNTs.

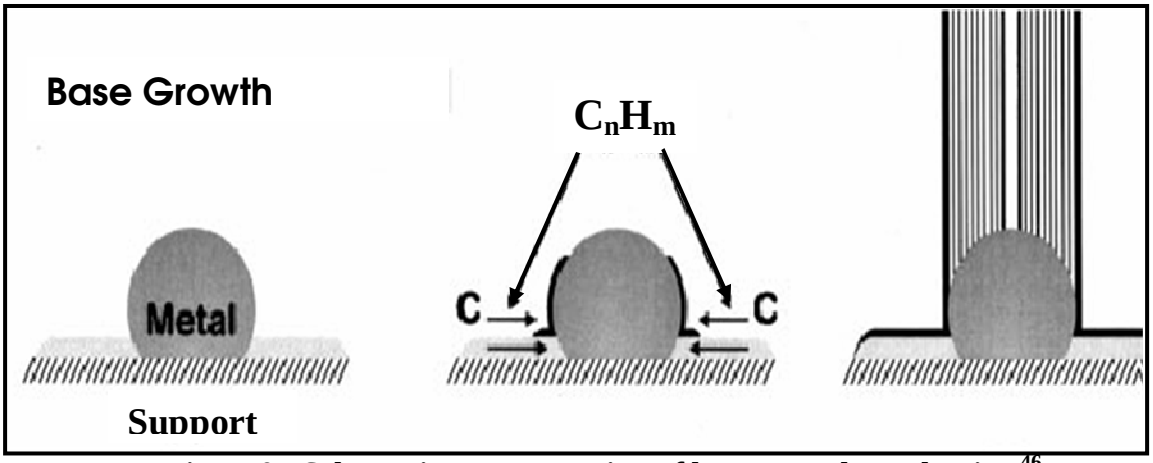

Fig.1.10: Schematic representation of base growth mechanism[46].

(b) Tip growth mechanism

When there is a weak interaction between the metal and the support then the growth of CNT follows this mechanism. In this case the metal particle which is loosely bonded to the support will be lifted by the carbon source molecule and the catalyst remains at the tip of the developing nanotube.

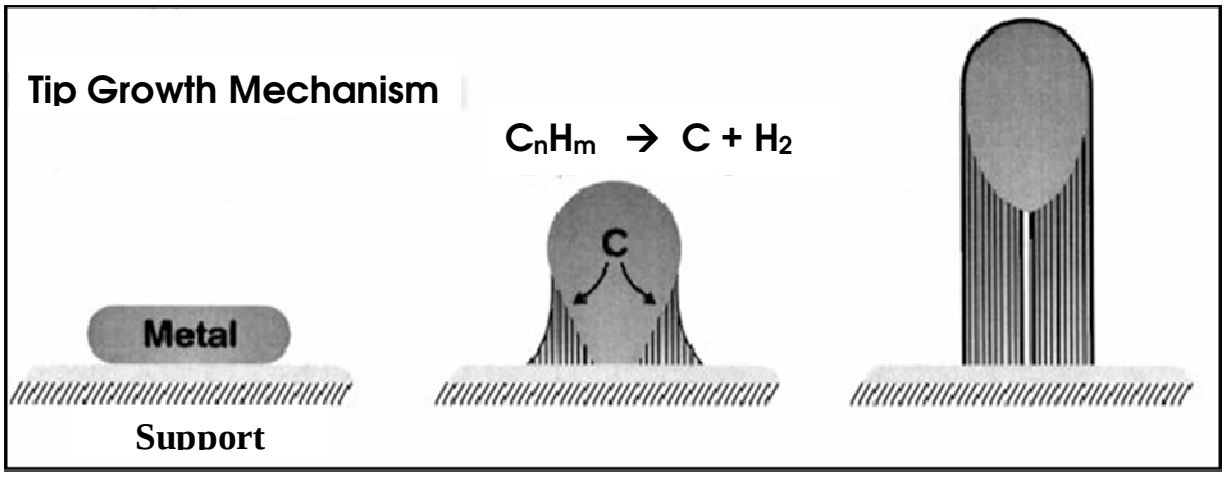

Fig.1.11: Schematic representation of the tip growth mechanism[46].

Tip growth mechanism is represented schematically in Fig: 1.11, initially the carbon precursor gas approaches the metal catalyst particle and undergoes decomposition at the contact of the metal and support. Thus, formed metastable carbon diffuses through the metal particle, simultaneously lifting the metal catalyst particle, as there exists a weak interaction between the metal and the support. Then the tube grows continuously by using the metastable carbon which is formed by the decomposition of the acetylene at the tip of the tube. This carbon diffuses through the metal catalyst particle and forms the inner walls of the multiwalled CNT as depicted in Fig.1.11. The diameter of the tube is also dependent on the size of the metal particle and the facet in which it is deposited over the support.

1.7 Field Emission

Field electron emission (FE) is a phenomenon involving the electric field induced emission of electrons from the surface of a condensed material, into vacuum or into another

material. This second material may be a gas, a liquid, or a non-metallic solid with low electrical conductivity. FE occurs at surface locations where the local surface electric field is particularly high. To generate significant amounts of emission, fields of 1 V/nm or more are required. The exact field needed depends both on the nature of the materials involved and on the amount of electron current being generated.

A simple model (the Fowler-Nordheim model) shows that the dependence of the emitted current on the local electric field and the work function is exponential-like. As a consequence, a small variation of the shape or surrounding of the emitter (geometric field enhancement) has a strong impact on the emitted current.

CNT as electron field emitters was already apparent from the first articles reporting extremely low turn-on fields and high current densities in 1995. Only a few studies followed during the next two years. From 1998 onwards, the perspective to use nanotubes as field emission devices spurred efforts worldwide: a first crude display as well as a lighting element was presented. Later studies addressed issues of large scale production compatible with microfabrication technology and strove towards better understanding of the emission mechanism.

CNT can be used as electron sources in two different types of set-ups, namely single and multiple electron beam devices. One possible application of a single electron beam instrument is an electron microscope that uses a single nanotube as a field emission electron gun to produce a highly coherent electron beam. Conversely, flat panel displays are the most popular example of multiple beam instruments where a continuous or patterned film of nanotubes provides a large number of independent electron beams [40].

As the field amplification increases with decreasing radius of curvature, for sharper tip it is the better. Nanotubes are thus ideally suited as field emitters, as their elongated shape ensures very high field amplification. Electron emission has already been observed on a single nanotube on application of a potential of 100V.

Electron sources are becoming increasingly important in research and everyday life. Although the conventional, thermoelectronic emitter seems to be declining, cold electron emitters using field emission show great potential for numerous applications.

CHAPTER 2

Experimental and Characterization Techniques

In this chapter, the experimental techniques used for growth and characterization of carbon nanotubes are discussed. Microwave plasma enhanced chemical vapor deposition (MPECVD) method was used for the deposition of these films. Scanning electron microscopy (SEM), Transmission electron microscopy (TEM), Energy dispersive X-ray spectroscopy (EDS), Raman spectroscopy and X-ray diffraction were used for the characterization of carbon nanostructures and catalyst nanoparticles.

2.1 Experimental set-up for Microwave Plasma Enhanced Chemical Vapour Deposition (MPECVD)

A tubular MPECVD set up was used for the deposition of nanostructured carbon films. The experimental set-up consists of a microwave generator, wave guide and tubular quartz tube. An aluminium cylinder was attached with the quartz tube. A rotary pump was used to maintaining pressure of the order ~10^{-2} Torr. The pressure was monitored by a pirani gauge. A set up of mass flow controllers (model 247 C MKS Instruments Inc., USA) with a 4-channel display was used to monitor and control the flow of reactant gases.

A quartz tube of ID = 40 mm, OD = 45 mm inserted vertically through a rectangular wave-guide as shown in fig 2.1. The lower end of the tube was attached to the aluminium cylinder and the upper end to the mass flow controllers. Substrate was placed in the middle of the quartz tube-waveguide intersection on a quartz tube made holder. The required substrate temperature was achieved by the microwave induction and the continuous collisions by the energetic plasma species. A window has been provided to view the plasma.

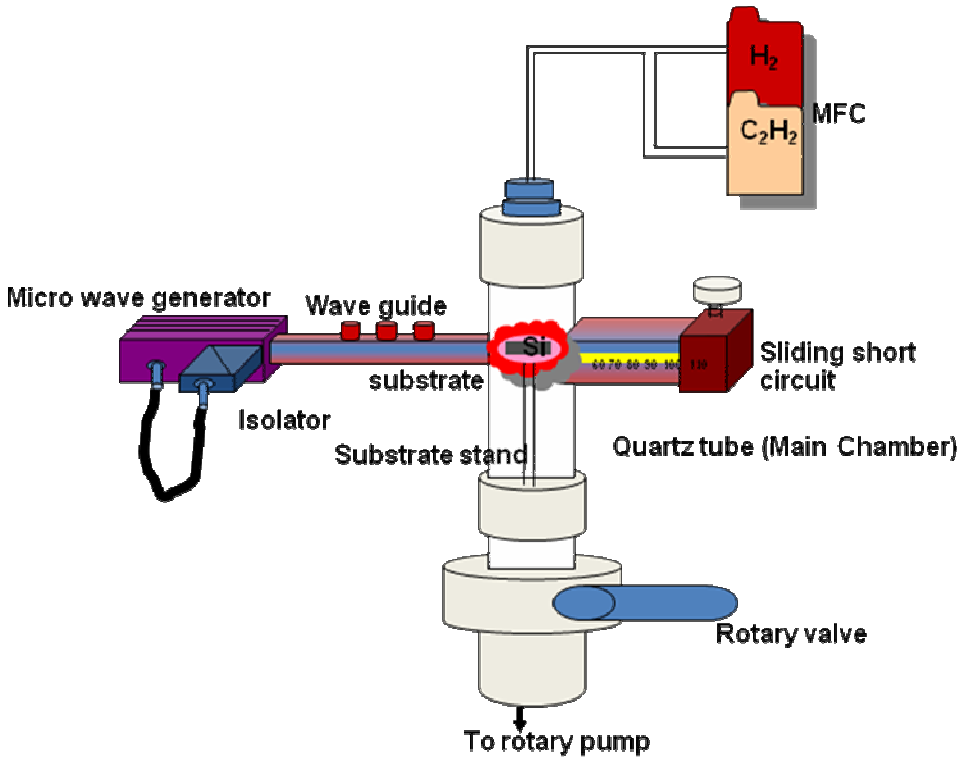

Fig.2.1: Schematic of MPECVD set up used for the growth of nanostructured carbon films

The microwave generator consists of a high voltage power supply (model GMP12KE, Sairem, France) with a maximum input power of 2.4 kW. The output of the supply was fairly stable and ripple-free. The output power can be varied by a 10-turn potentiometer. The power from the supply was fed to the microwave head through a high-voltage multiconductor cable connected to a magnetron which was capable of giving a maximum output power of 1.2 kW at a frequency of 2.45 GHz in continuous wave mode. The microwave head and the isolator were connected to the plasma cavity through a standard WR340 wave guide, a three stub tuner and a sliding short circuit.

Fig.2.2: Front view of MPECVD set up.

2.3 Experimental Procedure

Following steps were follows to clean the p-Si(100) substrates before deposition of thin films.

(a) Initially clean the p-Si(100) substrate were rinsed in 10 % HF solution in distilled water for one minute.

(b) Then they were cleaned ultrasonically using trichloroethylene, acetone and propanol.

Growth of nanostructure carbon film was carried out using following steps:

(1) Deposition of thin film of metal (Fe) on substrates by thermal evaporation technique. A thin film of cocatalyst (Ag) is deposited over Fe.

(2) Pretreatment of Ag-Fe-Si substrates in Ar and H_2 plasma in MPECVD system.

(3) Deposition of carbon films by introducing hydrocarbon (C_2H_2) in the plasma.

2.4 Characterization Techniques for carbon nanostructures

2.4.1 Electron Microscopy

Electron microscopy techniques have been found to be very useful for the analysis of the microstructure of carbon nanostructured materials. These techniques are explained as follows:

(a) Scanning Electron Microscopy(SEM)

SEM is a type of electron microscope that images the sample surface by scanning it with a high-energy beam of electrons in a raster scan pattern. The electrons interact with the atoms that make up the sample, producing signals that contain information about the sample's surface topography, composition and other properties such as electrical conductivity[47].

Figure 2.4 shows a schematic diagram of a SEM. The electron gun, which is the source of electrons, is usually a tungsten filament in the form of a hairpin which is directly heated. The resulting electron emission is accelerated by applying a variable potential between the grid cap and anode, which therefore changes the energy of the electron beam. Commonly, accelerating potentials from 1-40 kV are used. Alternative electron sources to tungsten hairpins are also available, the most usual being a rod of lanthanum hexaboride which can be directly or indirectly heated. LaB_6, electron sources produce higher brightness electron emission with a longer lifetime than tungsten filaments, but the vacuum requirements are more stringent.

The diameter of the electron beam formed by the gun is of the order of several micrometres which is far too large to be used for image formation. The beam diameter is demagnified by electromagnetic lenses (called condenser lenses) and focused by a third lens (the objective lens) into a spot having a diameter of a few nanometres. This small spot is scanned across the surface of a sample in the form of a raster by scanning coils housed inside the final lens. Interaction of the primary electron beam with the sample causes a variety of signals to be generated which can be detected and used to modulate the brightness of a cathode ray tube scanned in synchronization with the raster of the scanning beam[48].

Since the magnification of the image is the ratio of the length of a scanned line on the sample to the length of scanned image, magnification can be changed simply by adjusting the area over which the electron beam scans. The useful magnification range for a SEM is usually between about 15 X and 200000 X, thus allowing comparisons to be made with a simple visual examination as well as very high magnification imaging. Secondary electrons are detected by means of a positively biased scintillator which attracts the low energy electrons and turns them into light. The signal is transmitted via light guide to a photomultiplier and then the amplified and processed signal is used to modulate the brightness of the display cathode ray tube.

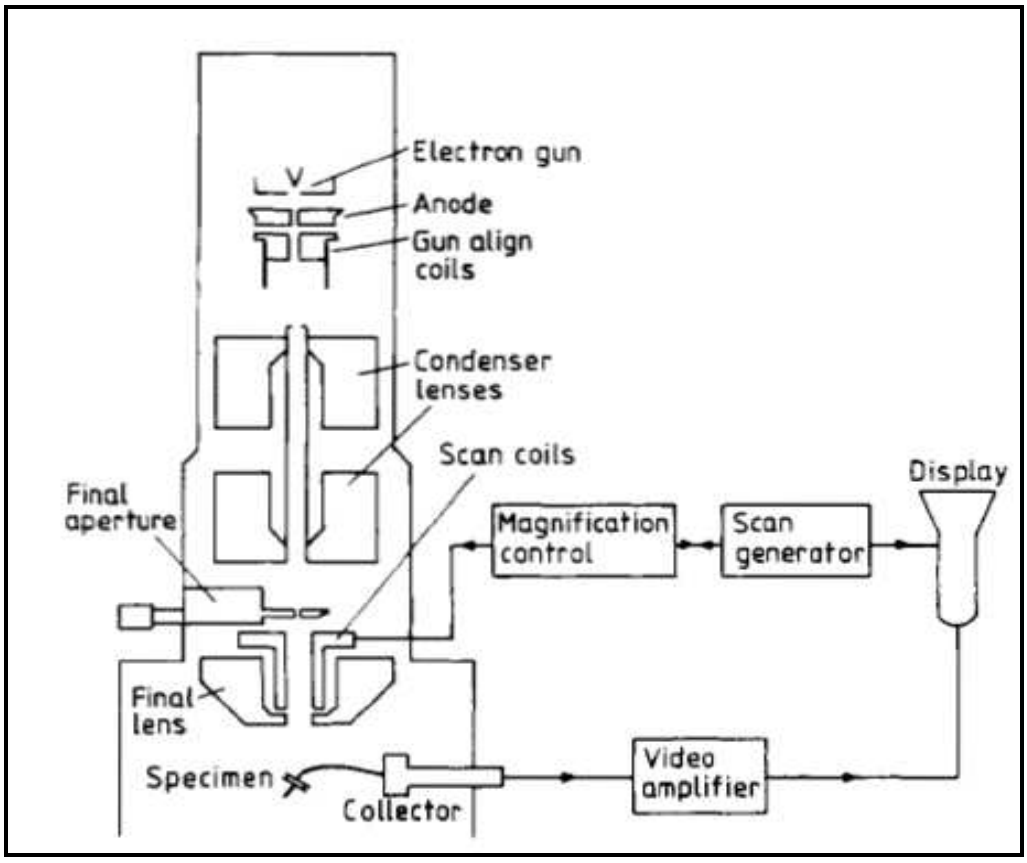

Fig.2.3: Schematic diagram of the Scanning Electron Microscope[48].

SEM is very useful technique for topographic study in SWNTs as well as MWNTs films[49]. With the help of SEM, density, diameter, and length of aligned CNTs can be estimated. Typical resolution of SEM is about 5 nm and can be used to image single

individual MWNT. This technique can also be used to determine the amount of impurities such as amorphous carbon or carbon coated catalyst particles coexisting with CNTs samples within the limits of resolution.

(a) Transmission electron microscopy(TEM)

TEM is a technique in which a beam of electrons is transmitted through an ultra thin specimen, interacting with the specimen as it passes through. An image is formed from the interaction of the electrons transmitted through the specimen; the image is magnified and focused onto an imaging device, such as a fluorescent screen, on a layer of photographic film, or to be detected by a sensor such as a CCD camera.

TEM are capable of imaging at a significantly higher resolution than light microscopes, owing to the small de Broglie wavelength of electrons. This enables the instrument to be able to examine fine detail even as small as a single column of atoms, which is tens of thousands times smaller than the smallest resolvable object in a light microscope. TEM forms a major analysis method in a range of scientific fields, in both physical and biological sciences[50].

Figure2.4 shows the schematic diagram of TEM and is constituted of: (1) two or three condenser lenses to focus the electron beam on the sample, (2) an objective lens to form the diffraction in the back focal plane and the image of the sample in the image plane, (3) some intermediate lenses to magnify the image or the diffraction pattern on the screen. If the sample is thin (< 200 nm) and constituted of light chemical elements, the image presents a very low contrast when it is focused.

The high resolution transmission electron microscope (HRTEM) image is an interference pattern between the forward scattered and the direct electron beams from the specimen. In the present study, TEM (CM 12) was operated generally at 120kV. HRTEM (TECNAI 20UT, 200 kV) was used for the lattice imaging.

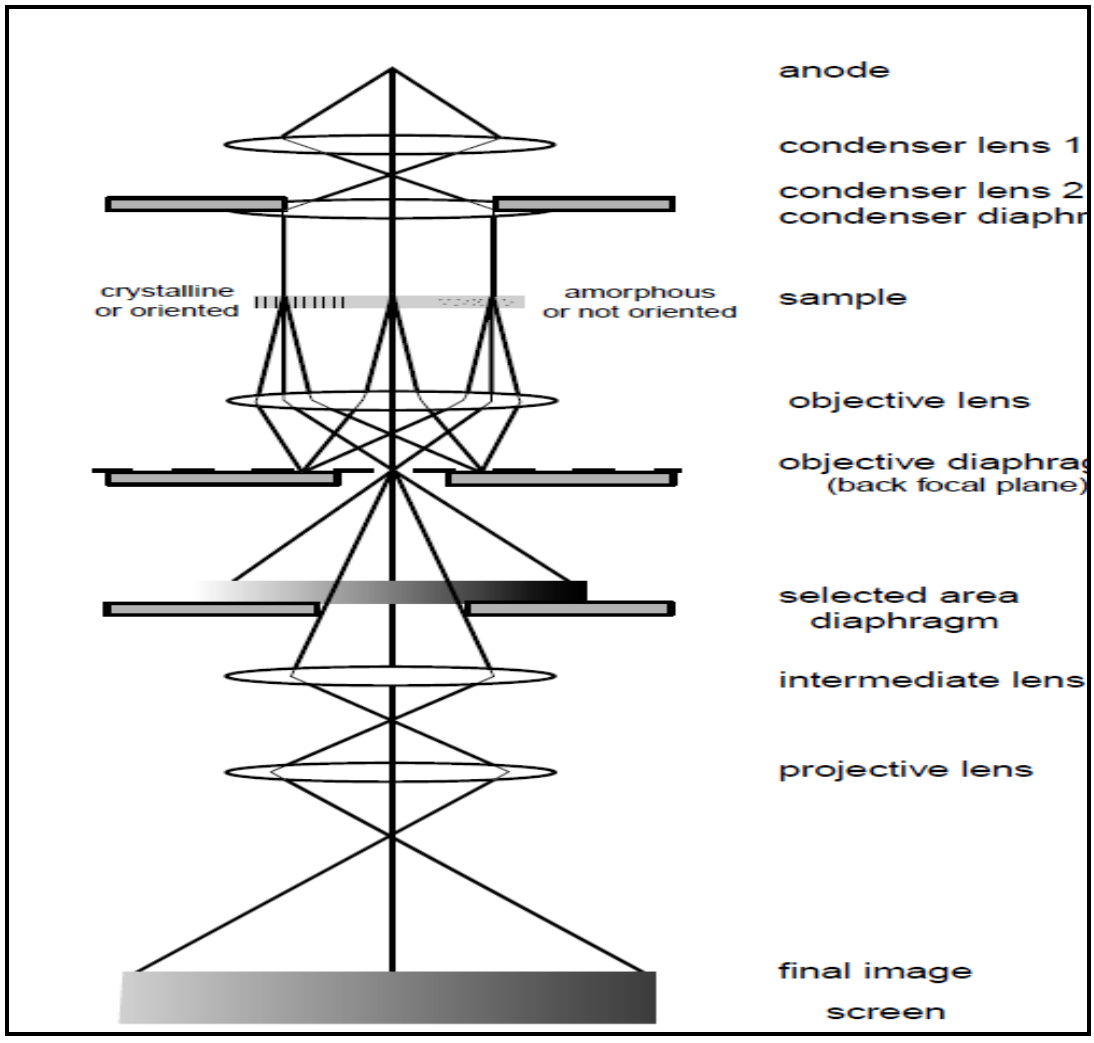

Fig.2.4: Schematic diagram of the conventional Transmission Electron Microscope imaging mode[51].

To obtain an amplitude contrast image, an objective diaphragm is inserted in the back focal plane to select the transmitted beam (and possibly few diffracted beam): the crystalline parts in Bragg orientation appear dark and the amorphous or not Bragg oriented parts appear bright. This imaging mode is called bright field mode (BF),as shown in Fig. 2.5 (a). If the diffraction is constituted by many diffracting phases, each of them can be differentiated by selecting one of its diffracted beams with the objective diaphragm.

For this, the incident beam must be tilted so that the diffracted beam is put on the objective lens axis to avoid off axis aberrations, Fig.2.5 (b). This mode is called dark field mode DF. The BF and DF modes are used for imaging materials to nanometer scale[51, 52].

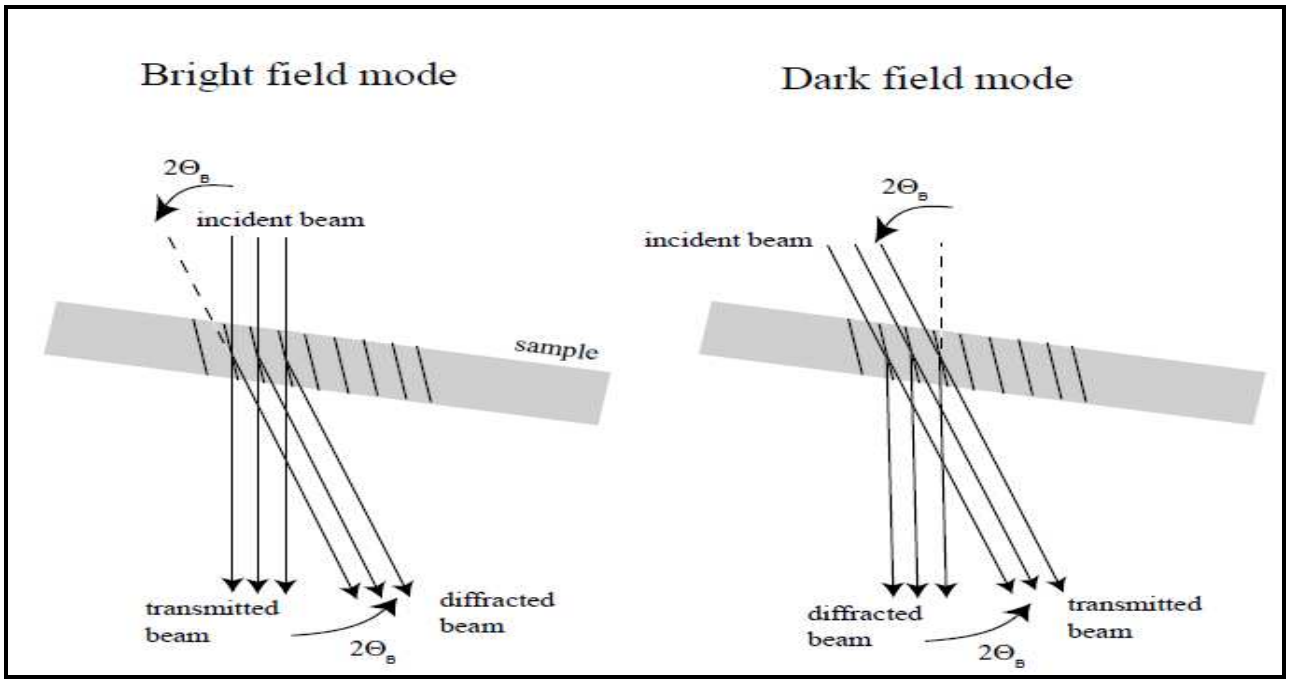

Fig.2.5: Schematic representation of (a) Bright field mode (b) Dark field mode.

Both conventional TEM and analytical TEM was used for the microstructural analysis of CNT samples. By using conventional TEM, the inner diameter, internal microstructure, compartment length of the CNTs and their growth modes were investigated. For TEM specimens, carbon film was peeled off from the substrate and ultra-sonicated in acetone from 10-20 minutes. Few dropes of this suspension were then placed on carbon coated copper grids. The grid was then mounted on the specimen holder and examined in the microscope.

2.4.2 Energy Dispersive X- ray Spectroscopy (EDX)

EDS was used for elemental study of the nanotubes and the particles embedded inside CNTs. The EDS spectra were recorded at an operating voltage of 200 kV, probe size 15 nm using low background double tilt holder and GENESIS software for data acquisition.

The basic principle involves the measurement of energy and intensity distribution of X- ray signals generated when an electron beam strikes a specimen. The X- rays emitted are used to identify the chemical composition of the specimen. The energy of each X- ray photon is characteristic of the element which has produced it. The X- ray peak positions, along the energy scale, identify the elements present in the sample. Th detector used in the EDS uses a lithium drifted silicon detector. This detector is operated at liquid nitrogen temperatures.

When an X- ray beam strikes the detector, it generates photo electrons within the body of silicon which generates electron- hole pairs. The electrons and holes are attracted to the opposite ends of the detector under a strong electric field and produce a current pulse the magnitude of which depend on the number of electron- hole pair created, which in turn depends on the energy of the incoming X- rays. Thus an X- ray spectrum can be acquired giving information on the elemental composition of the material under examination. All elements above Li may be detected with an acquisition time of ~100 seconds.

2.4.3 Raman spectroscopy

Raman spectroscopy is a spectroscopic technique used in condensed matter physics and chemistry to study vibrational, rotational, and other low-frequency modes in a system[53]. It relies on inelastic scattering, or Raman scattering, of monochromatic light, usually from a laser in the visible, near infrared or near ultraviolet range. The laser light interacts with phonons or other excitations in the system, resulting in the energy of the laser photons being shifted up or down. The shift in energy gives information about the phonon modes in the system. Infrared spectroscopy yields similar, but complementary, information Typically, a sample is illuminated with a laser beam. Light from the illuminated spot is collected with a lens and sent through a monochromator. Wavelengths close to the laser line, due to elastic Rayleigh scattering, are filtered out while the rest of the collected light is dispersed onto a detector.

The phenomena underlying Raman spectroscopy can be described by comparison with infrared spectroscopy as shown schematically in Fig.2.6. The primary event in infrared absorption is the transition of a molecule from a ground state (M) to a vibrationally excited state (M*) by absorption of an infrared photon with energy equal to the difference between the energies of the ground and the excited states. The reverse process, infrared emission, occurs when a molecule in the excited state (M*) emits a photon during the transition to a ground state (M). In infrared spectroscopy, one derives information by measuring the frequencies of infrared photons that a molecule absorbs and interpreting these frequencies in terms of the characteristic vibrational motions of the molecule. In complex molecules, some of the frequencies are associated with functional groups that have characteristic localized modes of vibration[54].

As is also shown in Fig.2.6, the same transitions between molecular vibrational states (M) and (M*) can result in Raman scattering. A key difference between the Raman and infrared processes is that, in the former process, the photons involved are not absorbed or emitted but rather shifted in frequency by an amount corresponding to the energy of the particular vibrational transition. In the Stokes process, which is the parallel of absorption, the scattered photons are shifted to lower frequencies as the molecules abstract energy from the exciting photons; in the anti-Stokes process, which is parallel to emission, the scattered photons are shifted to higher frequencies as they pick up the energy released by the molecules in the course of transitions to the ground state.

To be active in the infrared spectra, transitions must have a change in the molecular dipole associated with them. For Raman activity, in contrast, the change has to be in the polarizability of the molecule. These two molecular characteristics are qualitatively inversely related. A Raman spectrum is obtained by exposure of a sample to a monochromatic source of exciting photons and measurement of the frequencies of the scattered light.

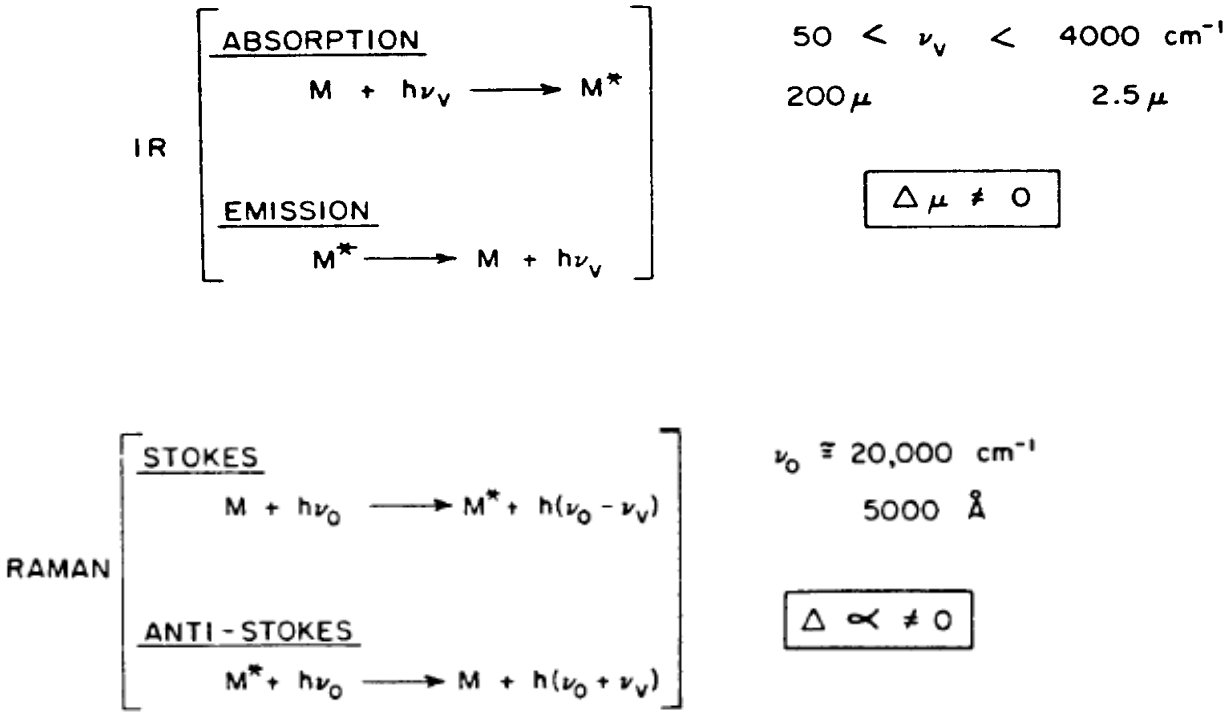

Fig.2.6: A comparison of infrared and Raman phenomena; μ= dipole moment, ν_v= vibrational frequency, ν_0= exiciting frequency.

Because the intensity of the Raman scattered component is much lower than the Rayleigh scattered component, a highly selective monochromator and a very sensitive detector are required. The exciting photons are typically of much higher energies than those of the fundamental vibrations of most chemical bonds or systems of bonds, usually by a factor ranging from about 6 for O—H and C—H bonds to about 200 for bonds between very heavy atoms, as for example in 12. The 514.5 and 488 nm lines from an argon ion laser are often used as exciting frequencies[55].

A typical Raman system consists of the following basic components: (1) an excitation source, usually a laser; (2) optics for sample illumination; (3) a double or triple monochromator and (4) a signal processing system consisting of a detector, an amplifier, and an output device. A diagram showing various components of the Raman spectrometer is shown in Fig. 2.7. A number of stages are involved in the acquisition of Raman spectrum. A sample is mounted in the sample chamber and laser light is focused on it with the help of a lens.

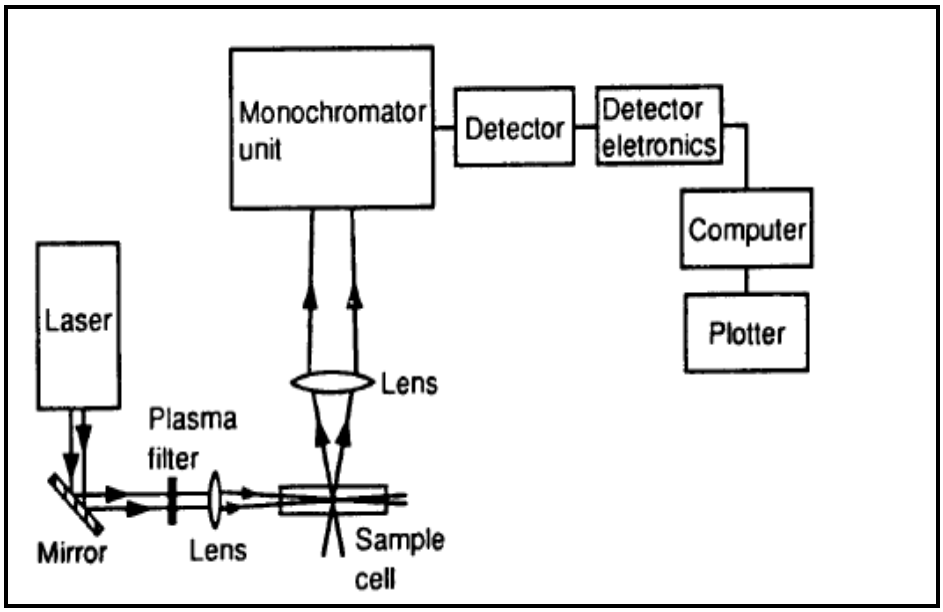

Fig.2.7: Schematic diagram of Raman Spectroscopy.

In a conventional Raman system using a photomultiplier tube (PMT) detector, light intensity at various frequencies is meusured by scanning the monochromator. A plot of signal intensity against wavenumber constitutes it Raman spectrum.

2.4.4 X-ray Diffraction

X-ray diffraction (XRD) is a versatile, non-destructive technique that reveals detailed information about the chemical composition and crystallographic structure of natural and manufactured materials. For thin films GAXRD is used.

By glancing angle X- ray diffraction(GAXRD) it is possible to study the structural properties of the thin films as well as the near the surface region of materials. XRD has been used for the investigation of the structure of SWNT bundles and MWNTs[56,57]. The XRD data for the MWNTs exhibits a dominant peak at ~26.2^0 which is attributed to the reflection from the layered structure of the MWNT.

In the present study GAXRD is used to confirm the graphitic nature of the carbon sample along with phase of the catalyst materials used for the growth of nanostructured carbon films. A microprocessor controlled X- ray diffractometer (Philips) with CuKα radiation (λ= 1.5418A0) was used in the present study. The diffractometer is equipped with a 12 kW rotating anode with sample rotation facility. The sample rotation helps to expose all the planes to the incoming X-rays, thereby avoiding the preferential orientation effects. The schematic diagram of the GAXRD is shown in Fig: 2.8.

The X- ray beam from the source, narrowed by an incident slits, falls on the sample surface at glancing angle which could be varied from 0 to 10^o. X- rays diffracted from the sample surfac pass through the Soller slits, which limits the divergence of X-rays in the vertical direction by allowing only axial rays to pass through it. The signal then falls on a graphite flat single crystal, acting as beam monochromator. The signal was then fed to the photomultiplier tube interfaced to a computer which stores the data.

During measurements, the incident angle was kept constant (1^o in present study) and the sample was rotated in a vertical plane. The X- ray tube was operated at 4 kW using 100 mA current. The interplanar spacing (d) was determined using the Bragg's formula,

$$n.\lambda = 2d\sin\theta$$

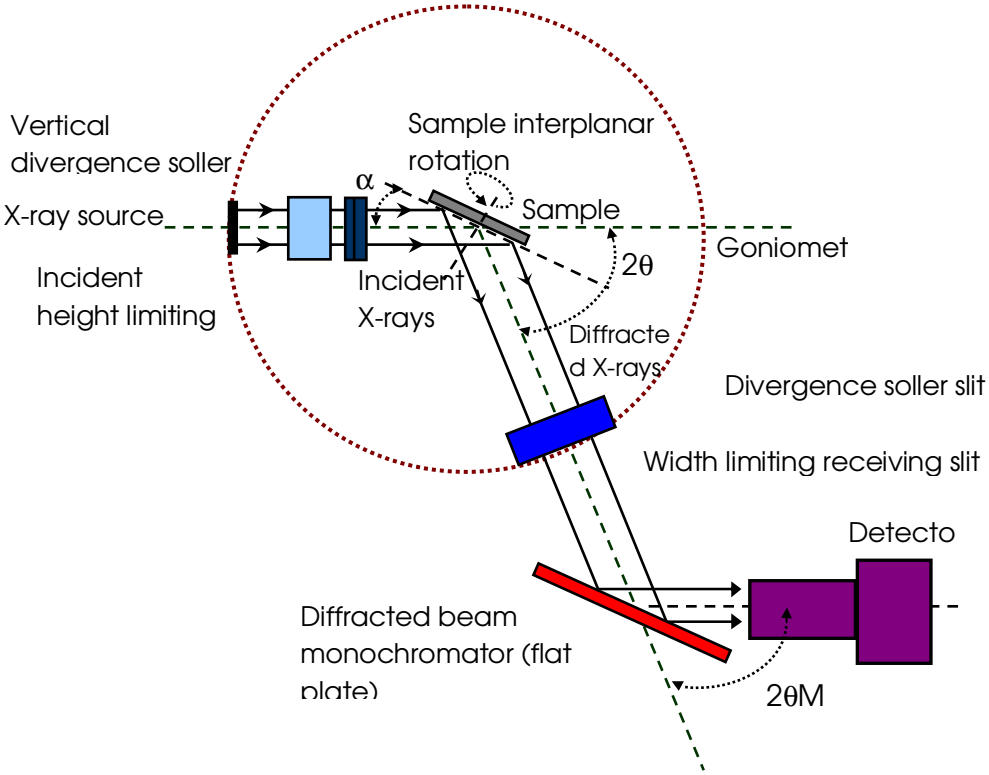

Fig.2.8: Schematic diagram of X-ray diffractometer.

Crystal structure was identified by comparing the experimentally observed d values with ASTM data cards and the reflections were indexed with proper Miller indices. Full width at half maximum (FWHM) of the XRD peaks was used to estimate the average crystallite size by using Scherrer's formula [58],

$$R = 0.9\lambda/\beta \cos\theta$$

Where R is the average crystallite size, β the FWHM of the most intense peak on the 2θ scale in the radians and λ the wavelength of the X- rays used.

CHAPTER 3

GROWTH AND CHARACTERIZATION OF CARBON NANOSTRUCTURES

In this chapter, growth of aligned carbon nanotubes films using C_2H_2-H_2 gas mixture with catalyst (Fe) and cocatalyst (Ag) over Si substrate, in microwave plasma enhanced CVD process, has been discussed. Growth of nanostructured carbon film having large density of uniformly distributed carbon nanowalls have been discussed under varying deposition time. XRD, SEM, TEM, Raman spectroscopy techniques were used to characterize these films.

3.1 Experimental details

(i) Deposition of catalyst layer

Iron (Fe) film of thickness ~ 10 nm was deposited on p-Si (100) substrate using thermal evaporation technique at a base pressure of 3.5 X 10^{-6} Torr. Another set of samples was prepared using a non catalyst Ag film of thickness ~6nm beneath the Fe catalyst film on p-Si(100) substrates by thermal evaporation technique.

(ii) Pretreatment of catalyst coated substrates

These substrates were kept inside the vacuum chamber of MPECVD system. The Fe and Fe-Ag coated substrate was pretreated in Ar plasma for 10 minutes at input microwave power of 550 W, followed by H_2 flow for 5 minutes. Formation of the nanoparticles due to plasma treatment is shown in Fig.3.1, which happens because of the heating the substrate by active plasma species. The hydrogen plasma etches out of Fe and Ag-Fe films and cleans the top surface of catalyst film. Under these conditions the substrate temperature was estimated to be ~600^0C.

(iii) Deposition of Carbon films

C_2H_2 gas was introduced into the chamber, using mass flow controller which acts as a precursor gas for the growth of carbon nanotubes. Samples with different growth time were deposited to study the time evolution of surface morphology named as F101, F102, F103.

Another set of samples was deposited on p-Si substrate, having an underlayer of Ag(~6nm thick) along with Fe(~10 nm thick) layer. These were prepared under the same conditions. Three samples named as A101, A102, A103 were deposited. The experimental parameters for these samples are listed in Table 3.1.

In order to study the effect of varying gas flow ratios of precursor C_2H_2 gas, five samples named A1, A2, A3, A4, A5 were prepared. The experimental parameters for these samples are listed in Table 3.3.

In this set, carbon films with varying growth time were deposited. Five samples named as A01, A02, A03, A04, A05 were deposited keeping the microwave power, deposition pressure, gas flow rates (C_2H_2: H_2 = 20: 80) constant. Table 3.4 gives details of the parameters used for this set of samples.

Initially a non catalyst Ag film of thickness ~6nm was deposited on p-Si(100) substrates by thermal evaporation technique as discussed above over this film, catalyst (Fe) film of thickness ~10 nm was deposited by thermal evaporation technique. These substrates were then used for the deposition of carbon nanostructures. These substrates were pretreated in Ar plasma for 10 minutes and then H_2 gas is introduced and after that for deposition acetylene gas (C_2H_2: Ar = 20: 80) to deposit carbon films maintaining total pressure at 5 Torr is introduced.

Table 3.1 Parameters used for the growth of nanostructured carbon films.

Parameters	**Pretreatment Conditions**	**Growth Conditions**
Microwave power	470 W	470 W
Substrate temperature	600 ^{0}C	600 ^{0}C
Pressure	5 Torr	5 Torr
Catalyst thickness (Fe)	10 nm	10 nm
Co catalyst thickness (Ag)	6 nm	6 nm
Gas	Ar+ H_2	C_2H_2 + H_2

Table 3.2 Growth parameters for samples deposited at different deposition time.

Sample F(Fe)&A(Ag)	Growth time (minutes)	Gas flow ratio
F101	1	15:75
F102	2	15:75
F103	3	15:75
A101	1	15:75
A102	2	15:75
A103	3	15:75

Table 3.3 Parameter used for the study of effect of gas flow ratios on the growth of CNT films.

Sample	Gas flow ratio (C_2H_2: H_2)	Growth time (min)
A1	10:75	1
A2	13:75	1
A3	15:75	1
A4	17:75	1
A5	20:75	1

Table 3.4 Parametres used for the study of effect growth time at constant microwave power on the growth behaviour of carbon nanowalls.

Sample	Growth time (minutes)	Gas flow ratio
A01	1	20:80
A02	2	20:80
A03	3	20:80
A04	4	20:80

3.2 Results and discussion

3.2.1 Effect of plasma Treatment on the Fe and Ag-Fe film

The Fe films deposited on Si substrates by thermal evaporation technique were continuous and smooth as shown in fig 3.1(a). However, after Ar and H_2 plasma pre-treatment, the continuous films converted into well-separated and quasi spherical particles as shown in Fig. 3.1 (b). The size of these particles varied from 20-100 nm. Breaking of continuous Fe film into nanoparticles is due to the continuous collisions of active ions in the plasma with the film and due to heating in the microwave plasma the Fe nanoparticles agglomerate and become isolated bigger nanoclusters.

Fig3.1(c) shows the nanoparticles of Fe deposited film with an underlayer of Ag. The size of nanoparticles in this case varied from 45-75nm.

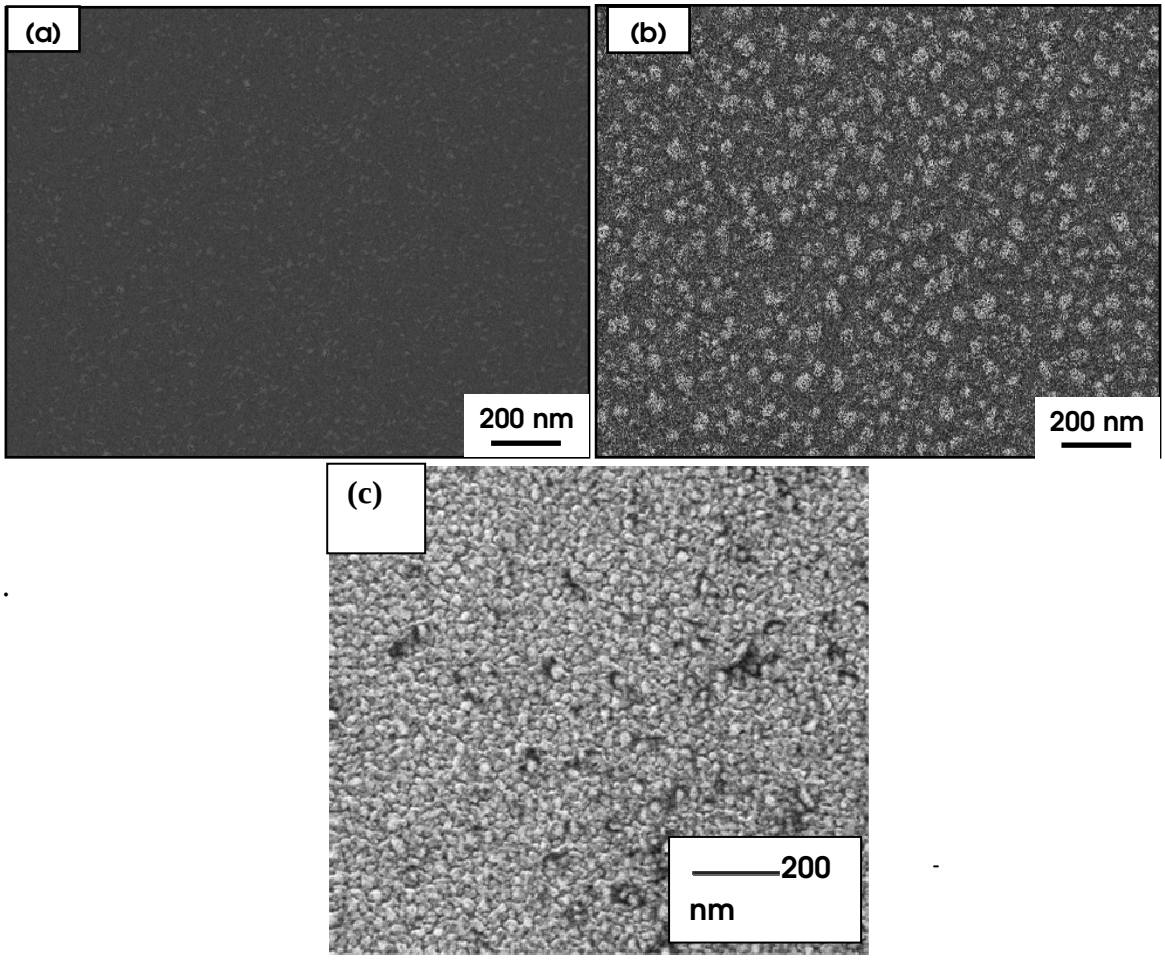

.

Fig. 3.1: SEM micrograph of Fe film (a) as deposited and (b) after plasma pre-treatment showing formation of nanoparticles (c) Ag-Fe film after plasma pre-treatment.

3.2.2 EDX studies

It was important to study the distribution and formation of Ag and Fe nanoparticles after plasma heat treatment. It was expected that Ag would restrict the agglomeration of Fe nanoparticles because of negligible solubility of Ag in Fe and vice-varsa. This results is controlled separation between Fe nanoparticles which is important for the growth of CNTs. Figure 3.2 shows the EDX spectrum of Ag-Fe nanoparticles after plasma heat treatment. The spectrum confirms the presence of Ag nanoparticles and Fe nanoparticles. The presence of Cu peak is due to the Copper grid used for mounting the sample and oxygen peak may be due to oxidation of the surface of grid. The encircled red spot in figure shows the location choosen for obtaining the EDX spectra

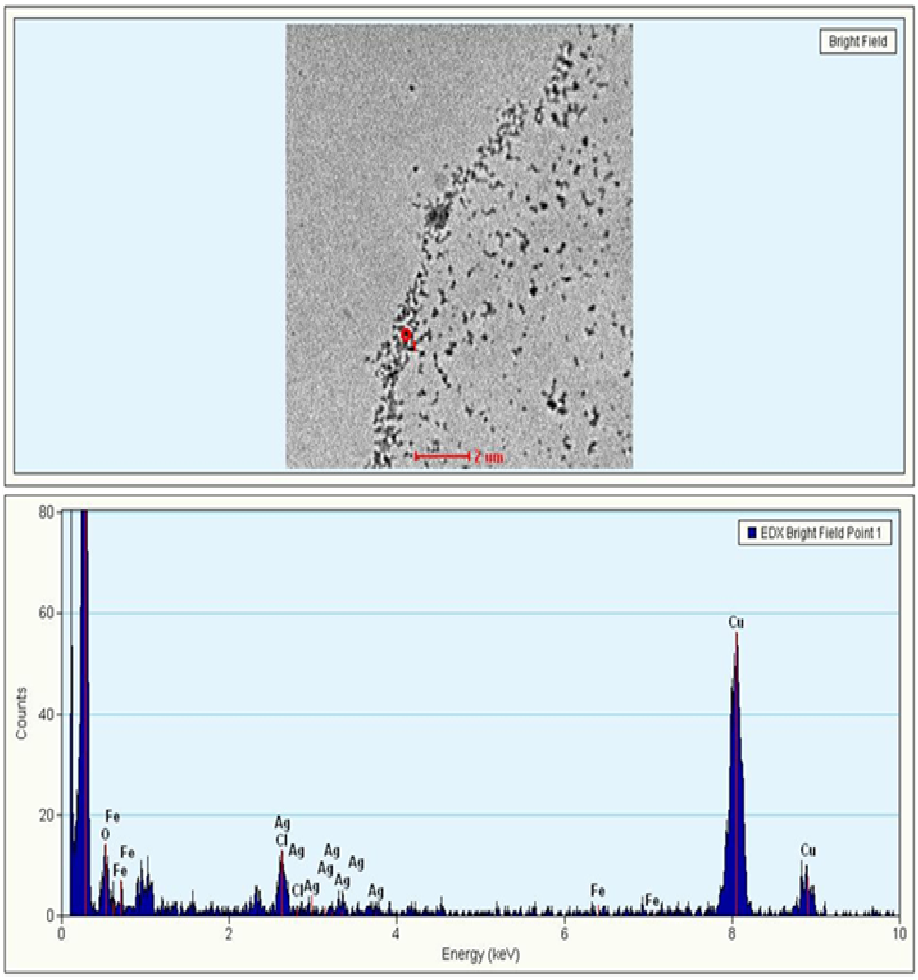

Fig.3.2: EDX spectra of catalyst Fe with an underlayer of Ag nanoparticles.

3.2.3 HRTEM studies of Ag-Fe nanoparticles

Fig 3.3 shows carbon coated nanoparticles in which size of Fe nanoparticles varies from 35 – 75 nm.

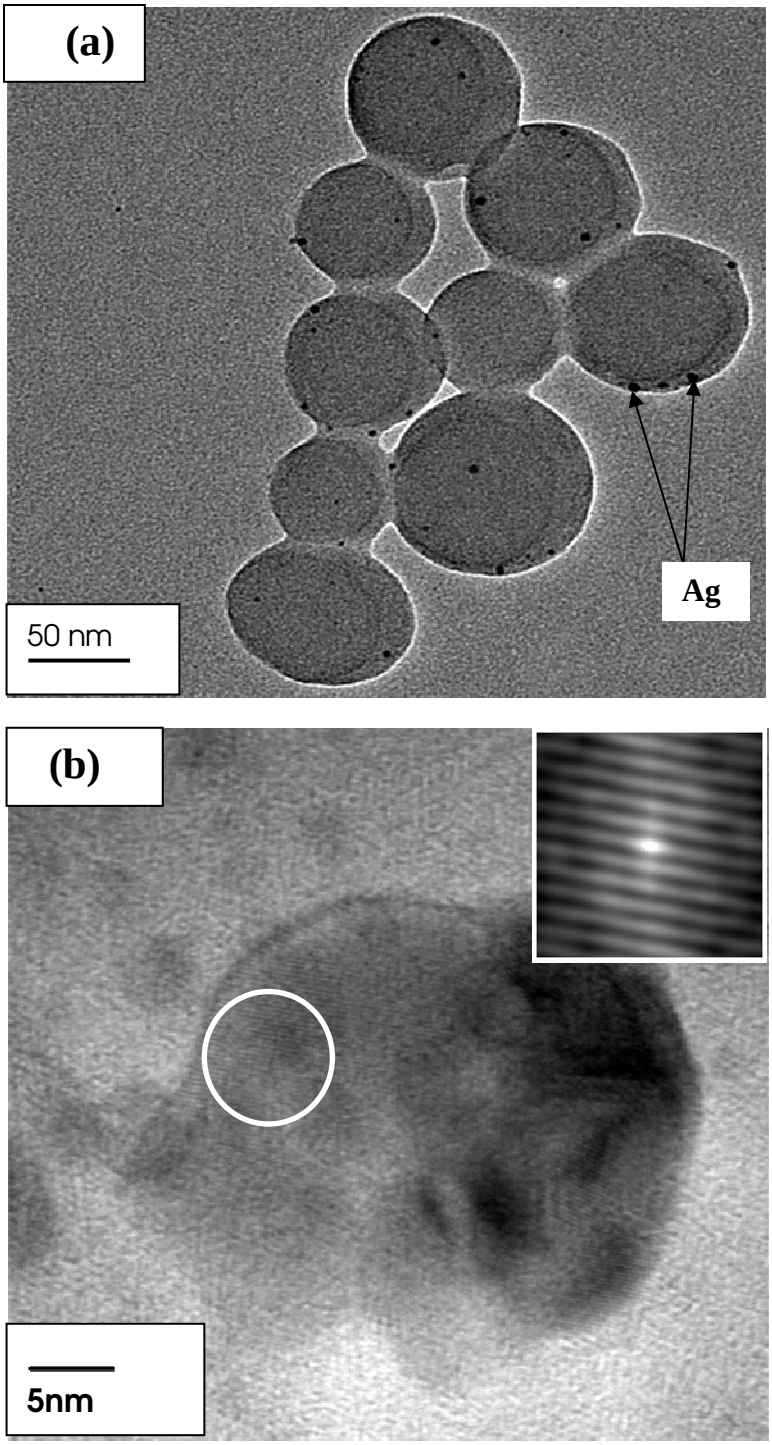

Fig.3.3: TEM micrograph of nanoparticles of pre-treated Ag-Fe film.

From figure it can be easily seen that there is variation in contrast of nanoparticles. The smaller particles are dark while the larger ones are lighter. From HRTEM analysis, the small dark size particles are silver particles of plane (111). Small sized Ag particles are observed dispersed in the matrix of larger sized Fe which is confirmed from the HRTEM analysis. The d-spacing is corresponds to 0.232 nm which is of Ag(111) plane shown in the inset.

3.2.4 XRD Studies

The typical XRD pattern of the Ag-Fe nanoparticles (fig 3.1(c)) is shown in Fig. 3.4. Strong peak at ~23.0^0 corresponds to the silicon which was used as a substrate. The low intensity peak at ~38.0^0 is due to the Ag (111) plane. The low intensity broader peak at ~44.0^0 may be attributed to the bcc Fe (110). It is clear from XRD pattern that there is no alloy formation between Fe and Ag.

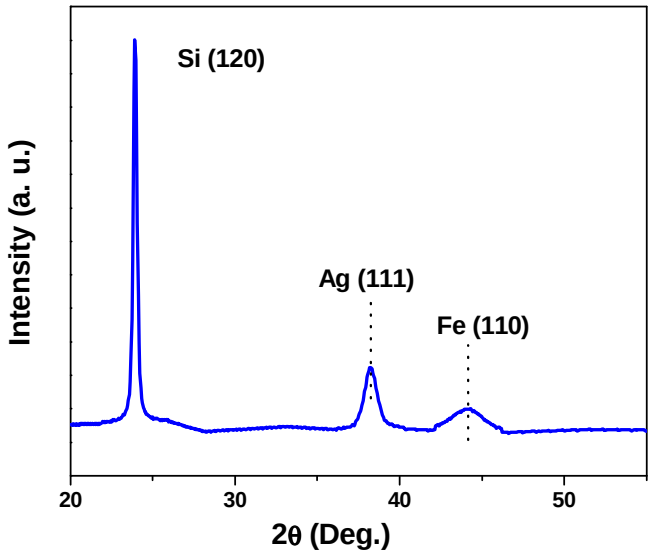

Fig.3.4: GAXRD of sample after heat treatment.

3.2.5 Carbon nanostructures deposited over Fe and Ag–Fe catalyst layer

Fig. 3.5 shows SEM micrographs of Ag-Fe deposited film and Fe deposited film. Surface morphology is clear from the micrographs. The density of carbon nanostructures is more for sample A101 (Fig 3.5i(a)) as compared to F101 (fig.3.5i(b)) sample. This may be due to well separated Fe particles when an underlayer of silver is present increases the

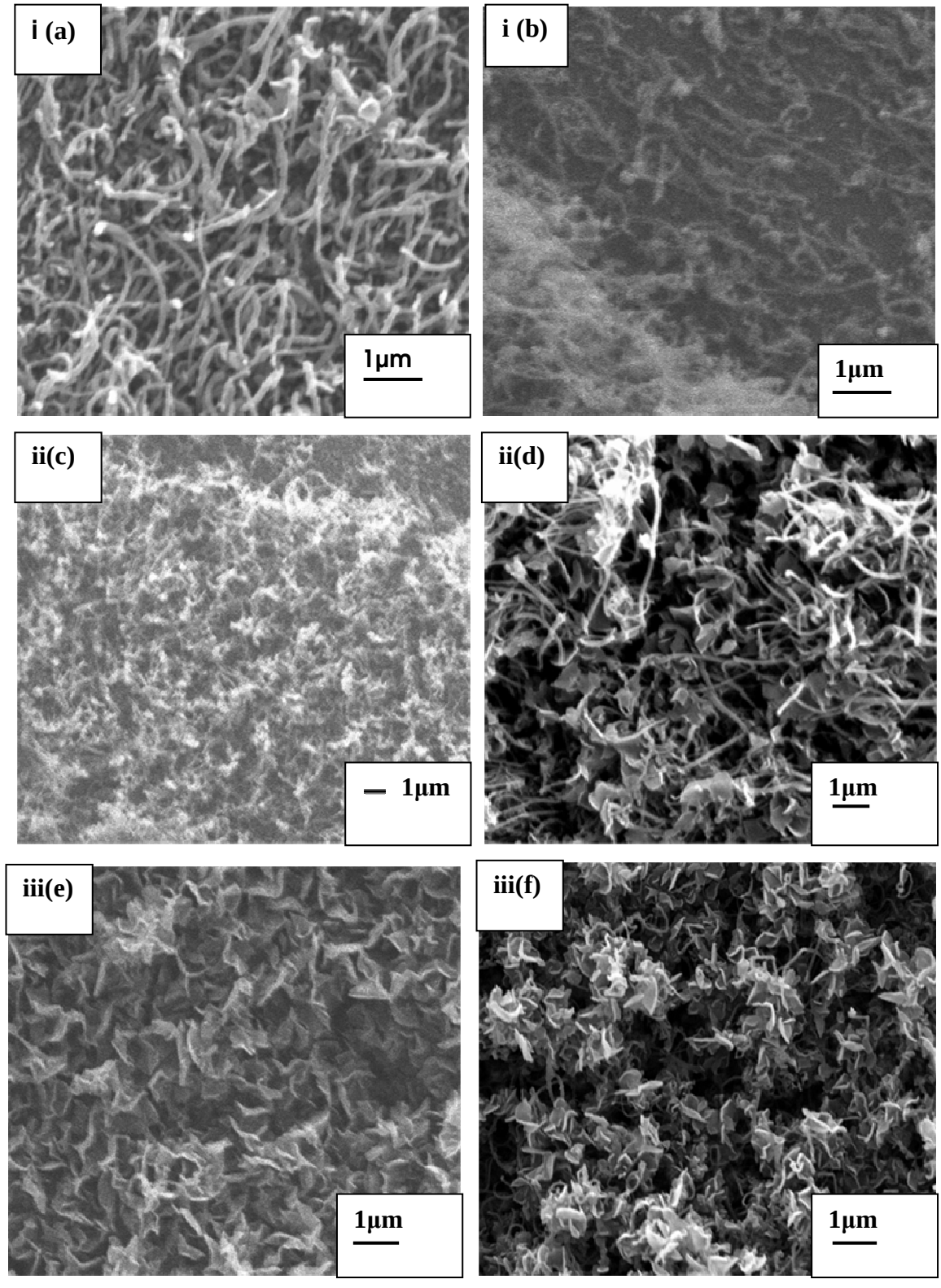

Fig.3.5: SEM micrographs of carbon nanostructures over Ag-Fe and Fe catalyst for i(a,b) 1 min ii(c,d) 2 min iii(e,f) 3 min

Number of reactive sites[59] which promote to 1-D carbon nanostructure growth, while in case of only Fe film, due to the formation of iron silicide, less amount of 1-D carbon nanostructure are formed because it hinders the 1-D carbon nanostructure growth. Formation of iron silicide is proved by the XRD spectra. As the deposition time is increased, highly dense 1D structure are obtained as shown in figure 3.5ii(c). For sample F102 some CNTs are present at the base and top surface consists of flakes (fig.3.5ii(d). With further increase in deposition time flakes are obtained for both samples A103 and F103 shown in fig. 3.5iii(e,f). In other words as the deposition time increases the catalyst particles get deactivated due to decomposition of excess carbon over their surface thereby leading carbon nanoflakes.

3.2.6 TEM Studies

Fig 3.6(a) shows the TEM micrograph of sample A101. The outer diameter of CNTs was found to be 19-39 nm while inner diameter was 6-17 nm. Fig 3.6a (ii) shows a single nanotube and it consists of many hollow compartments of unequal length. Each hollow compartment has inner diameter is maximum at its base and decreasing towards the tip (fig 3.6a (ii). The length of nanotube varies from 600 nm to 1.7 μm. For sample F101 the TEM micrograph shows that the length of CNTs is typically 500 nm and the inner and outer diameters are varying from 6-12nm and 13-38 nm respectively [fig3.6 (b(ii)].

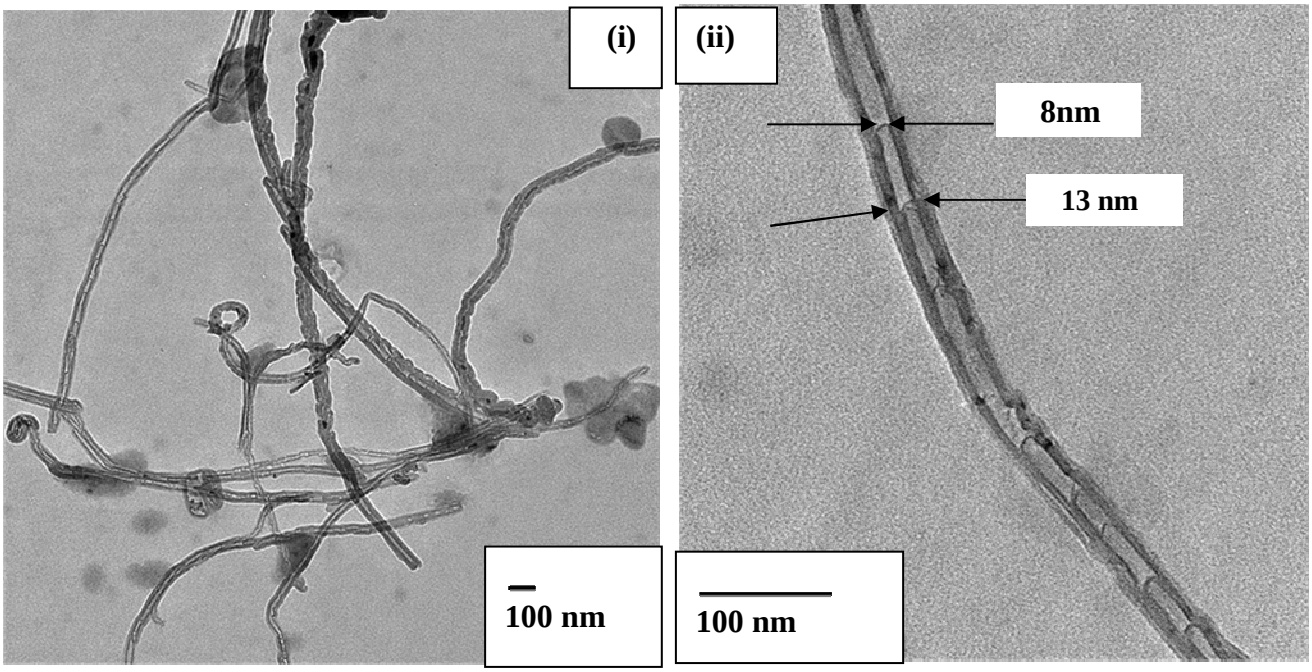

(a)

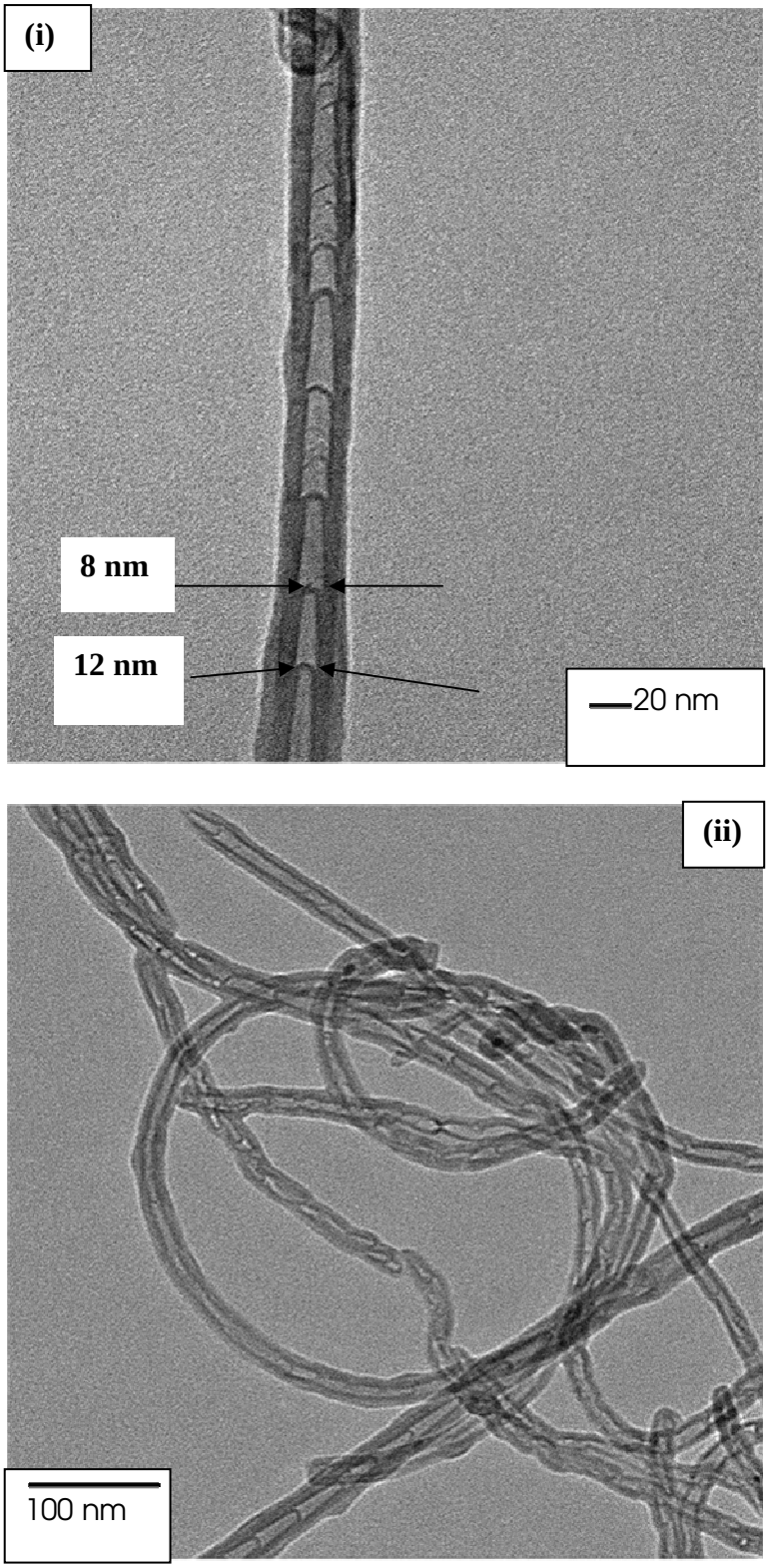

(b)

Fig 3.6 TEM mcrographs of sample (a) A101 and (b) F101

TEM micrograph of sample A102 and F102 is shown in figure 3.7 (a) and (b). From TEM micrograph of sample A102 and F102 is shown in figure 3.7 (a) and (b). From TEM micrographs we found that the inner diameter of sample A102 varied from 4-21 nm and outer diameter 18-31 nm and impurities are present on the sidewalls due to higher concentration of carbon and for sample F102 the inner diameter of tube varied from 7-19 nm and outer 18-28 nm and here spiral shaped nanotube is formed. It is speculated that, due to presence of stress the breaking of catalyst (Fe) particles takes place and the different position of catalytic particle are shown in fig.3.7 (b).

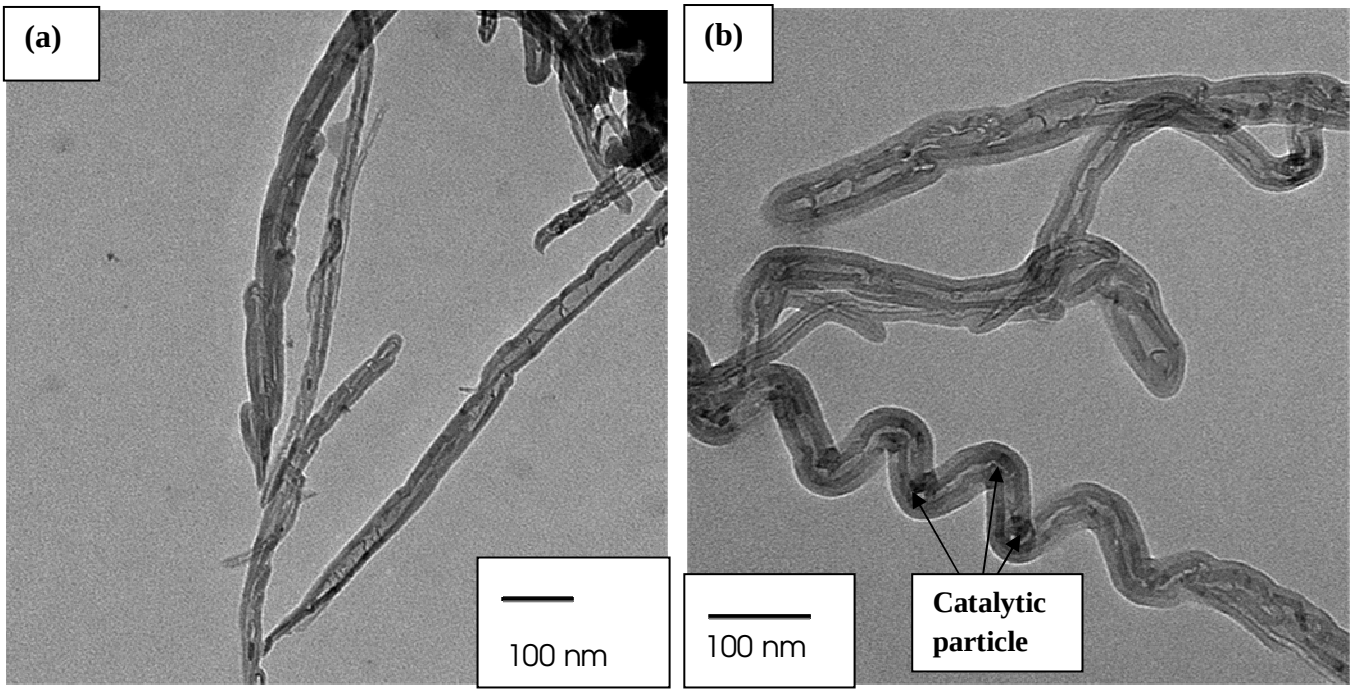

Fig.3.7: TEM micrograph of sample A 102 (a) and F 102 (b)

3.2.7 GAXRD Studies

The typical GAXRD pattern of the sample A101 and F101 is shown in fig 3.8(a) and (b) respectively. It is clear from the fig 3.8 (a) that there is no alloy formation between Ag and Fe. Strong peak at ~ 26.3^0 indicates the presence of (002) planes of graphite. The peak at ~ 38.2^0 shows the presence of Ag (111) and low intensity peak at ~ 43.5^0 is attributed to Fe (110). The diffraction due to Si was found at ~ 52^0 corresponds to Si (103) which is used as substrate.

From fig 3.8 (b) the low intensity peaks observed between ~ 40-45^0 were due to Fe (110) and FeSi. The peak at ~ 26.2^0 indicates the presence of (002) plane of graphite and peak at ~ 56.0^0 corresponds to Si used as a substrate.

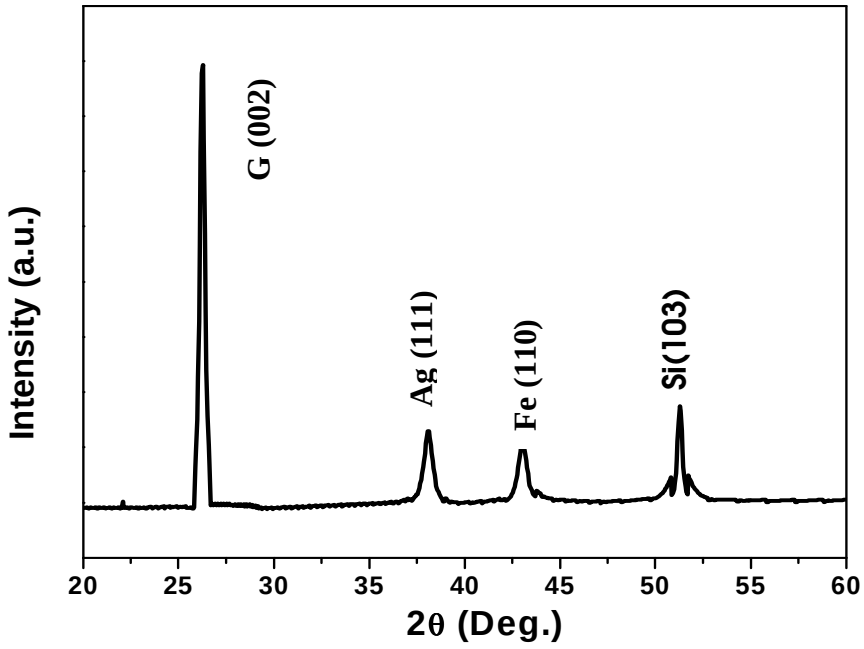

(a)

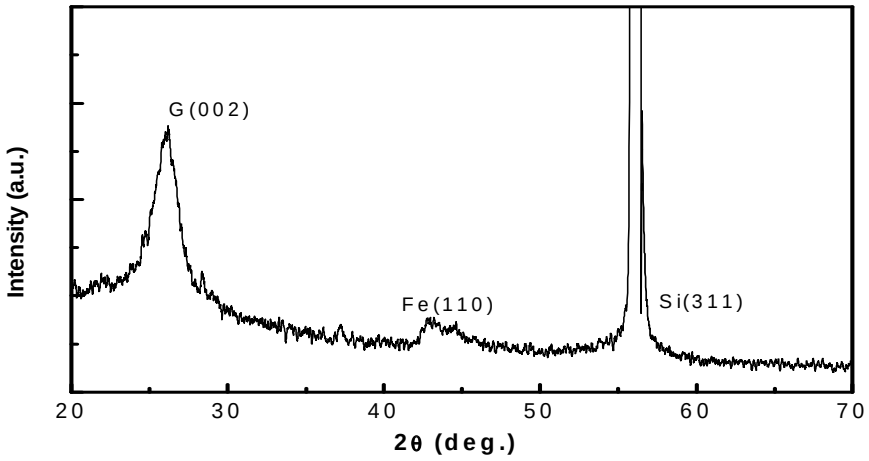

(b)

Fig.3.8: GAXRD of sample (a) A101 and (b) F101

3.2.8 Raman studies

The Raman spectrum for sample A101 and F101 from fig.3.9 (a) and (b) respectively shows the graphitic or G-band at ~ 1560 and 1564 cm-1 respectively and the defect induced D-band at ~ 1335 and 1328 cm-1. From fig 3.9 (b) it is clear that the MWNTs are having more defects due to larger D-band because this band corresponds to intrinsic defects.

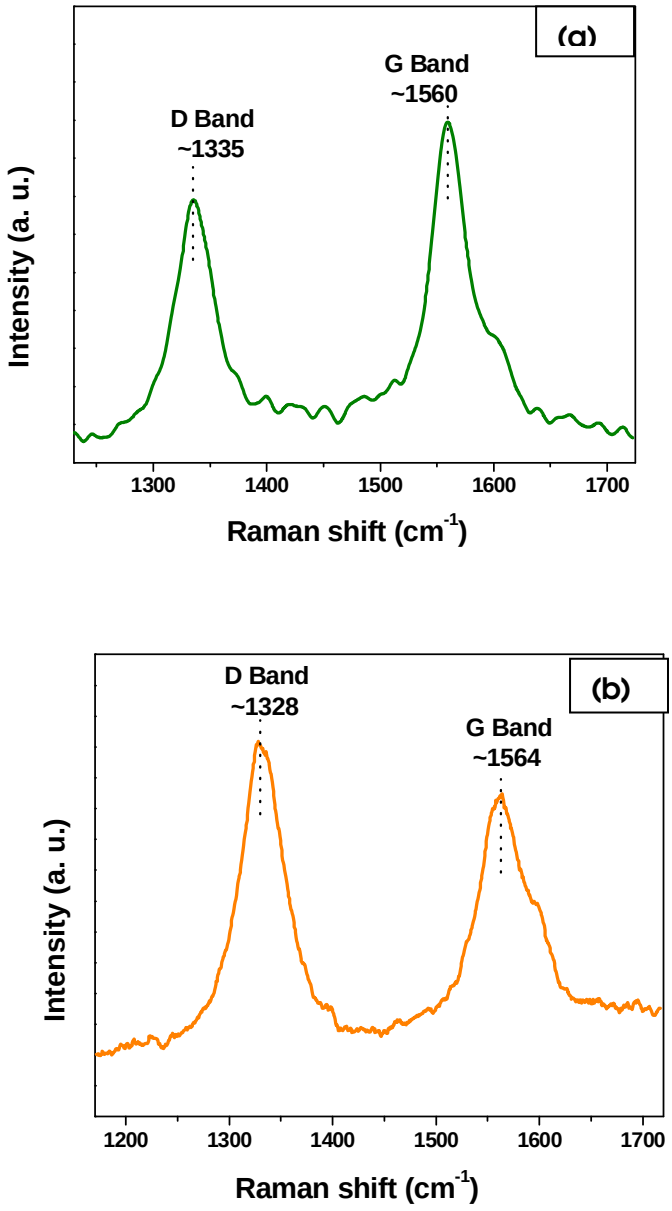

Fig.3.9: Typical Raman spectrum of sample A101(a) and sample F101 (b)

From Raman spectra we speculate that MWNTs which are formed on Fe catalyst without any underlayer are more defective as campared to MWCNTs grown on a co-catalyst Ag underlayer over Fe as shown in fig 3.9 (a) and (b).

For qualitative analysis of graphite-like structures, the intensity ratio of the D-band to the G-band is measured. For sample A101 I(D)/I(G) ratio is ~ 0.7 and for sample F101 ~ 1.08 suggesting that CNTs has a large number of defects while in case of using Ag underlayer they are less defective.

3.2.8 Growth of Carbon nanostructures by changing the gas flow ratio of C_2H_2

CNTs were deposited with different flow ratio of C_2H_2. Flow rate of C_2H_2 varied from 10 to 20 sccm while H_2 flow rate, deposition time, deposition temperature, and working pressure were kept constant as shown in table 3.2. Fig (3.10) shows the SEM micrographs of CNTs grown on varying concentration given in table 3.2.

From fig 3.10 (a) it was noticed that no 1-D structure growth was occurs in sample A1 (C_2H_2:H_2 flow ratio of 10:75) and randomly aligned 1-D structure were observed for sample A2 (fig.b) (with flow ratio 13:75). When the flow ratio was 15:75, high density of 1-D structure was observed (fig 3.10(c)) which are vertically aligned shown in inset (fig.3.10c).

Further increase in the flow ratio resulted distortion of 1-D structure, top surface consists of flakes and some CNTs are observed at the base as shown in fig 3.10(d). Flakes are formed when the flow ratio was 20:75 and no CNTs are grown.

At lower concentration of C_2H_2 nanotube growth may not occur because of very low concentration of carbon species and presence of high density of etching species. Further increase in the C_2H_2 flow, a balance is set up between carbon supply and etching species and hence CNTs were grown. Again increase in C_2H_2 flow ratio results increase in the concentration of carbon source and a overabundance of decomposition and not enough precipitation, results in amorphous carbon and 2-D growth of nanostructures. In our study the optimum flow ratio was found to be 15:75 for C_2H_2:H_2.

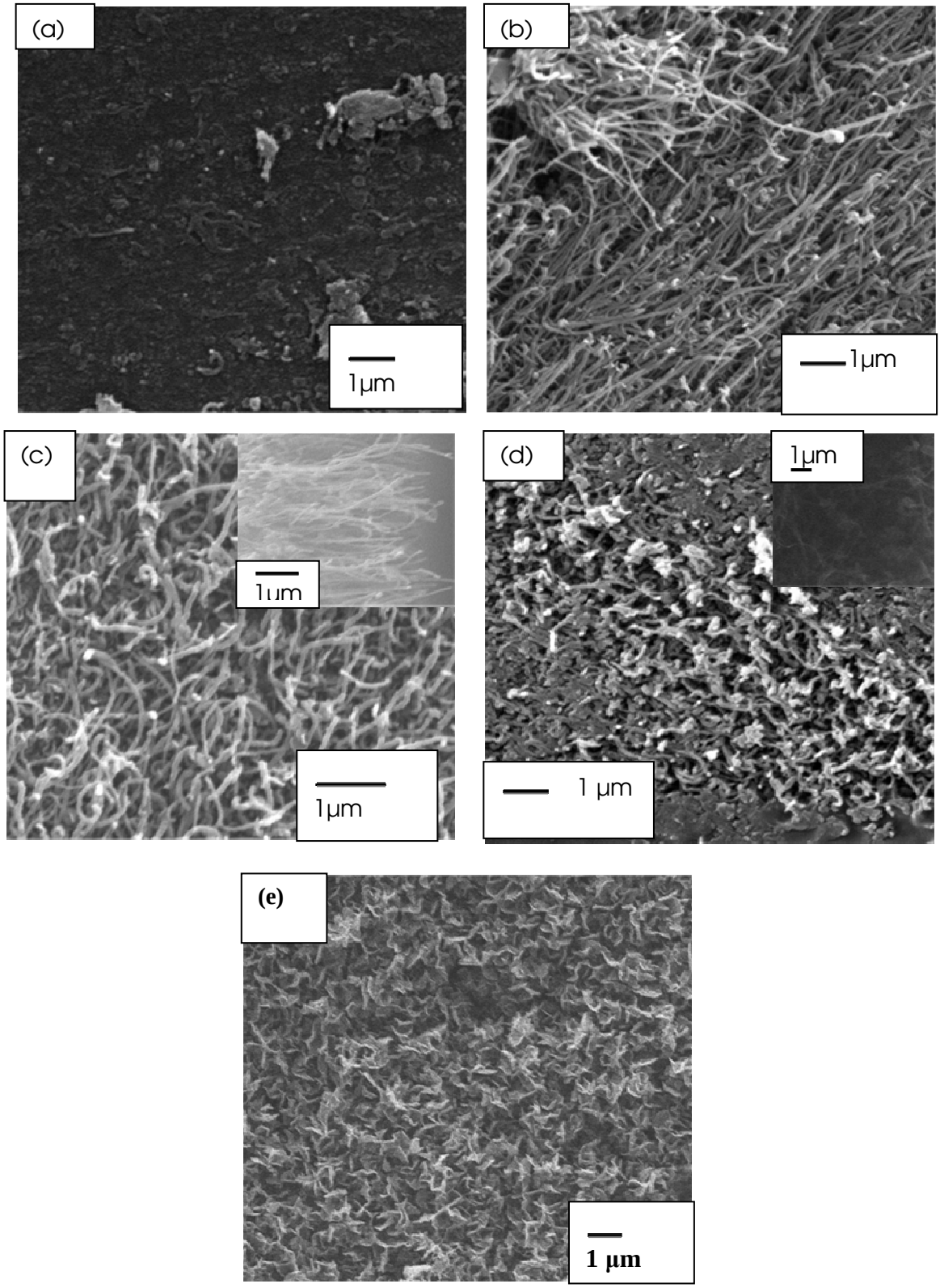

Fig.3.10: SEM micrographs of sample A1(a),A2(b),A3(c),A4(d),A5(e) with varying flow ratios

3.2.9 GROWTH AND STRUCTURE OF CARBON NANOWALLS

Results and Discussion

3.2.9.1 SEM Studies

The ~6 nm thick film of Ag-Fe coated on Si substrate was heated in Ar and H_2 plasma. The precursor gas was used for growing the carbon nanostructures. Fig.3.11 show the surface morphology of samples A01, A02, A03 and A04 respectively with varying deposition time from 1- 4 minutes given in table3.3. These carbon films consist of uniformly distributed nanowalls. These nanowalls with its sharp edges were pointing normal to the substrate. The catalyst islands are formed at the initial stage of the growth as shown in fig 3.11(a). It is clear from the fig 3.11(b)-(e) that, on increasing the growth time density of the nanowalls decreased while its size increased. Fig 3.11(f) shows the magnified view of sample A04.

The surface morphology after preheating were unlikely to be the main reason for the formation of nanowalls, because after the preheating, all the surfaces showed almost the same type of morphology–similar to fig 3.11 (a). If metal cluster size is larger than the diffusion length of the caron[60], then CNT growth cannot occur. Large catalyst particles or no catalyst promote the growth of 2D structure[61]. In our experimental conditions, Fe clusters are observed to be tightly packed after plasma treatment due to presence of non catalyst Ag thin barrier layer as shown in Fig 3.11(a). This resulted in 2D nanowalls growth and no 1D growth was observed.

It is speculated that, initially CNT growth takes place and abundant carbon radicals are not only dissolved and precipitated by the catalyst particles but are also inserted in the sidewalls of the tubes during CNT growth, thus forming 2D structures. It is believed that abundant carbon radicals rapidly terminate the CNT growth due to catalyst saturation and remaining carbon species are mainly inserted in the 2D structure originating in the vicinity of the CNT tips. This 2D structure grows longer and become a CNW layer on the top of the CNT.

An important observation during the discussed growth process is that without any external biasing the nanowalls grow almost normal to the substrate surface. This suggests that the growth of CNW could be influenced by the self bias potential established on the immersed substrate surface in the high density plasma, the field lines of which are invariably

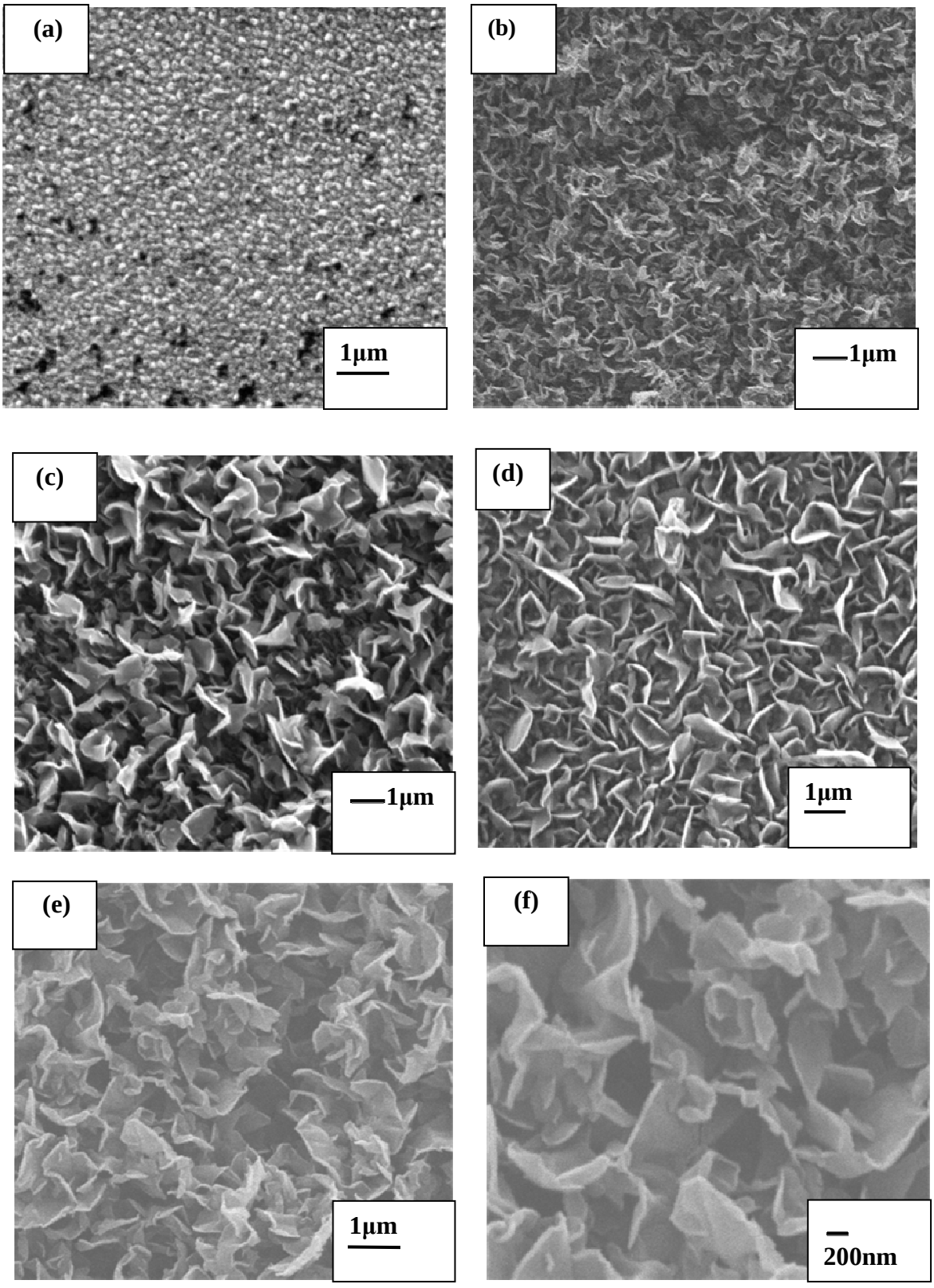

Fig.3.11: SEM micrograph of (a) H2 – plasma treated AgFe film and carbon films deposited at (b)1 (c) 2 (d) 3 (e) 4 minutes (f) magnified image of sample A05

terminated normal to the surface[62].The electrostatic force would force these carbon nanowalls to align with the field direction perpendicular to the substrate surface, an energetically most favourable orientation.

3.2.9.2 TEM Studies

Fig 3.12 shows the TEM micrograph of CNW along with CNT. From the fig 3.12 (a) it is clear that initially CNT are formed and then a continuous maze type structure are formed on top of the tips of the CNT. Higher magnification TEM micrograph of CNW is shown in the fig 3.12(b).Variation in contrast can be easily seen from the micrograph and dark contrast is due to corrugation of the CNW. A bamboo-shaped CNT together with CNW is shown in the fig 3.12 (c).

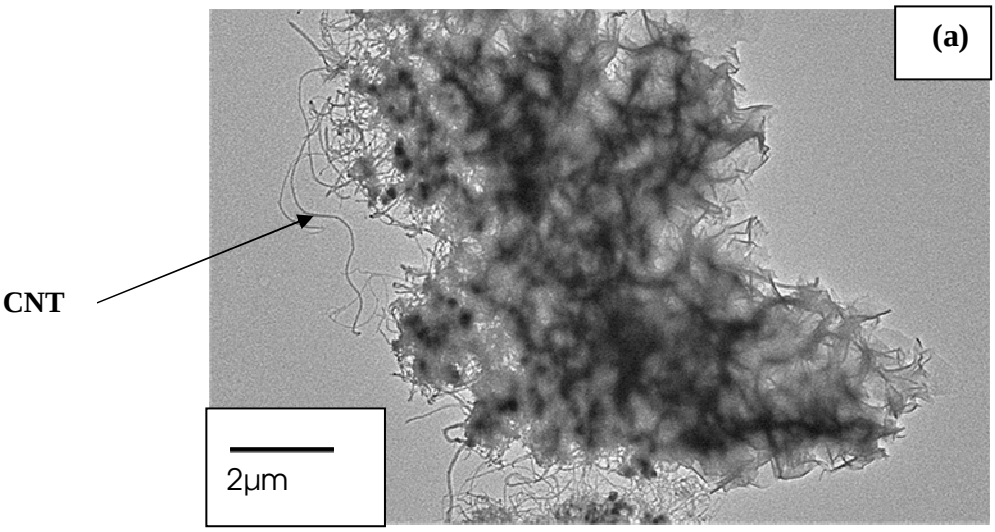

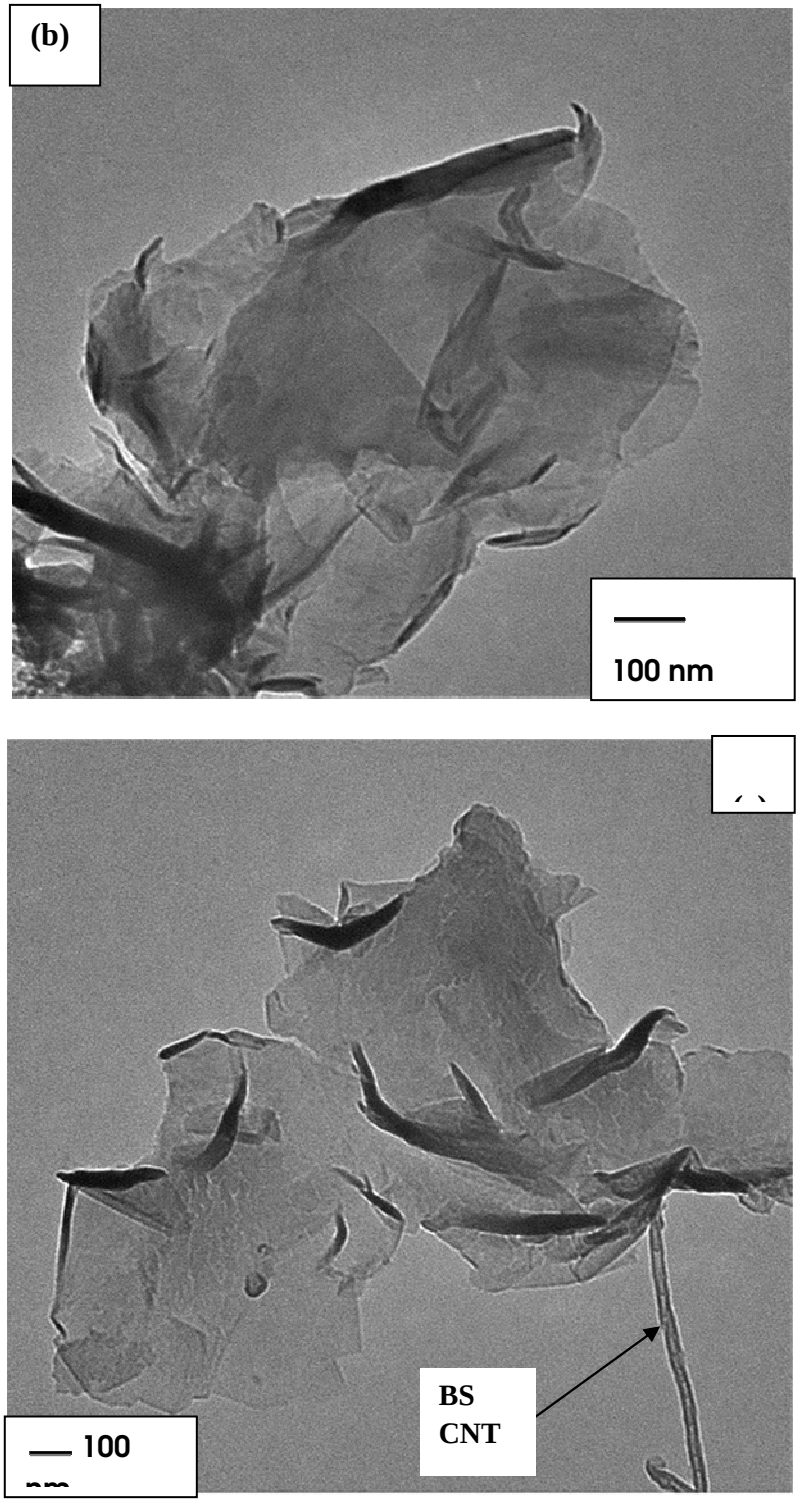

Fig.3.12: TEM micrograph of sample A04 (a) CNT with contiunous maze type structure (b) CNW with corrugating walls (c) BS CNT with CNW.

3.2.9.3 Crystallographic structure

3.2.9.3 GAXRD studies

Fig.3.13 shows typical X-ray diffractogram of carbon nanowalls.The peak at 26.0^0 corresponds to the (002) planes of graphite. The small intensity peaks are also observed at ~ 38.2^0 and at ~ 44.3^0 is corressponds to Ag(111) and Fe(110) respectively. This suggests that during pretreatment of Ag and Fe does not resulted any alloy formation.

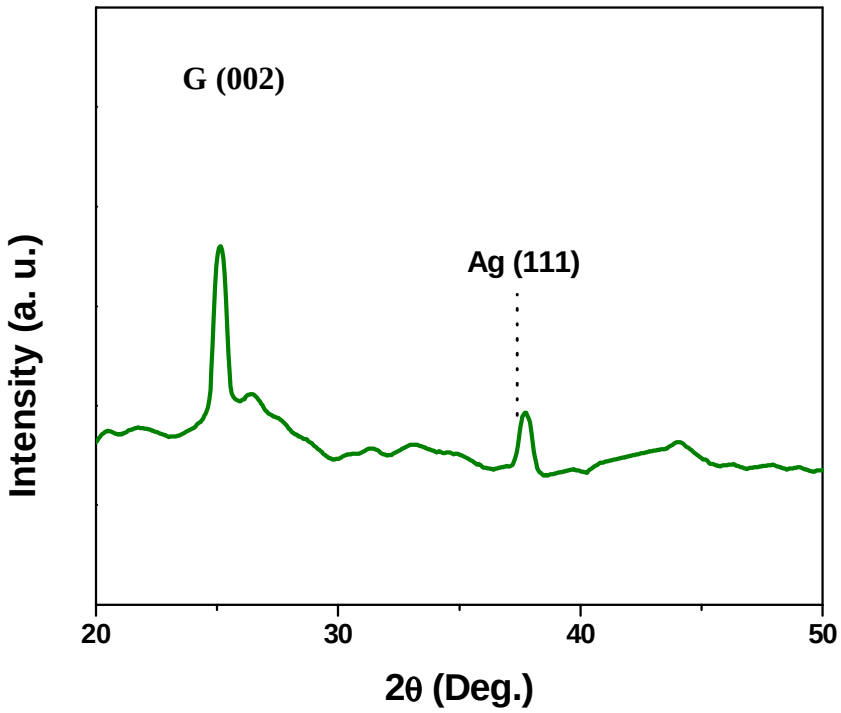

Fig.3.13: A typical X-ray diffractogram of carbon nanowall film.

3.2.9.4 Raman Studies

Fig 3.14 shows the first order Raman spectra of the sample A01 and A04 . Each spectra shows three charactristic spectra corresponds to graphite. For sample A02 two strong peaks at 1337 cm^{-1} and 1566 cm^{-1} are observed, which correspond to disorder induced D-band and G-band related to in plane sp^2 vibrations. Similarly peaks are observed at ~ 1340 cm^{-1} and 1569 cm^{-1} for sample A04. The peak at 1566 cm^{-1} falls well within the range of a

series of the peaks that have been observed for carbon nanotubes, and the disorder induced D'-band peak at 1607 cm^{-1}. CNW usually suffer from defects and are known for their relatively large intensity I(D)/I(G) ratio[63]. The I(D)/I(G) ratio for sample A02 was ~ 1.281 and for sample A05 ~ 1.06. Intensity ratio for sample A02 was more as campared to A05, which suggests, less defects.

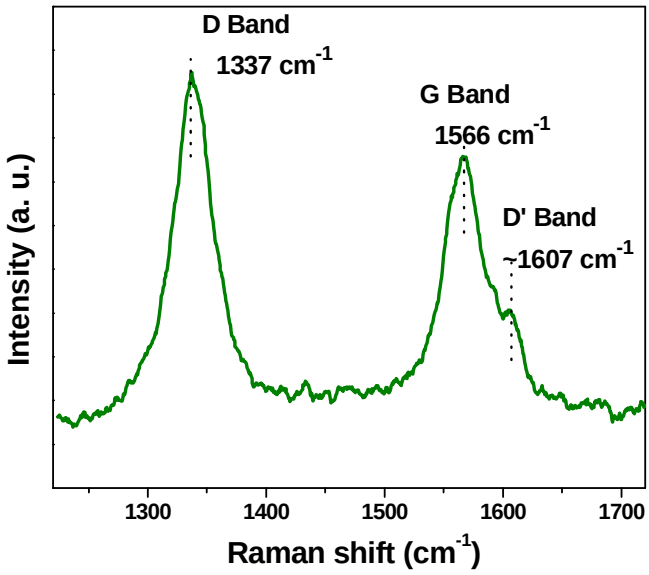

(a)

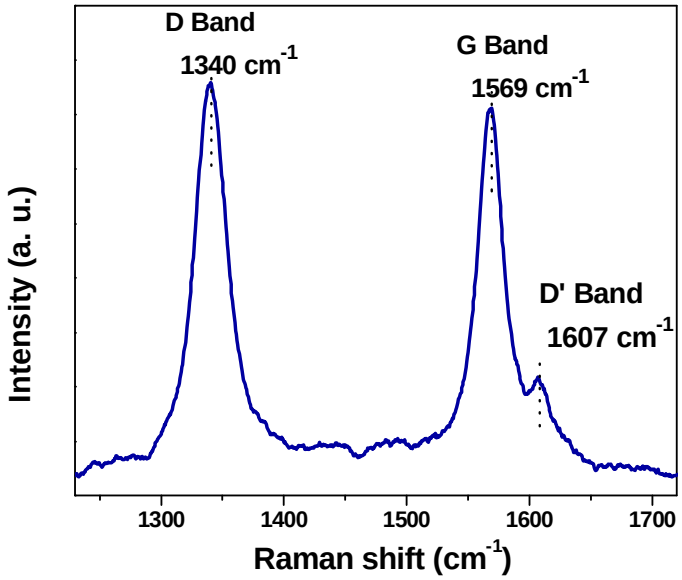

(b)

Fig.3.14: Raman spectra of sample (a) A01 and (b) A04

3.2.11 Effect of catalyst film thickness on the growth and microstructure of CNTs

SEM micrographs of Ag-Fe films with thickness of Ag film ~6 nm and ~10 nm respectively keeping the catalyst film thickness ~10 nm. Plasma treatment ($Ar+H_2$) for 15 minutes are shown in Fig.3.15(a,b). From figure it is clear that the size of particles was small for ~16 nm thick film while it become broader with increase the film thickness. The average particle size for ~16 nm and ~20 nm film was 45-75 nm, 130 – 240 nm respectively i.e. particle size increases with increase in film thickness. This could be attributed to the non uniform fragmentation of the Fe-Ag layer during $Ar+ H_2$ plasma treatment process and their agglomeration. The average particle size is much larger than the film thickness. Here a lot of tiny particles and Ag and Fe nanoparticles merge in one another and at different positions and due to this separation the growth of CNTs is faster. Due to faster growth they have no time to align themselves and will grow in any direction which results entangled growth of 1D carbon nanostructures.

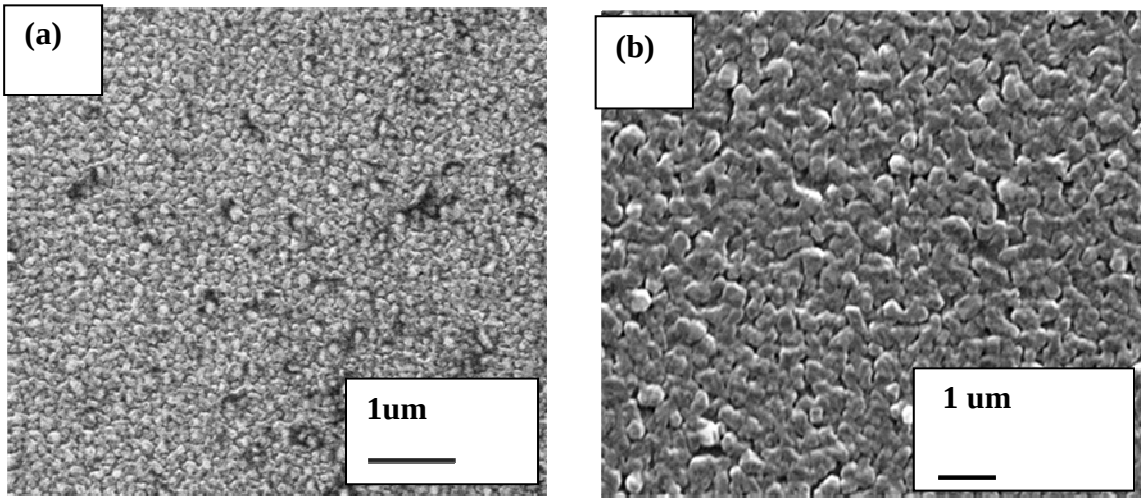

Fig.3.15: SEM micrograph of Ag and Fe film (a) 6 nm Ag (b) 10 nm Ag with 10 nm Fe film.

The CNT films grown on these substrates and their SEM micrographs are shown in figure 3.16. This shows that as the thickness of the film increases, the flakes are formed and base has some CNTs and when thickness is reduced then there is less formation of flaky structure on the top surface.

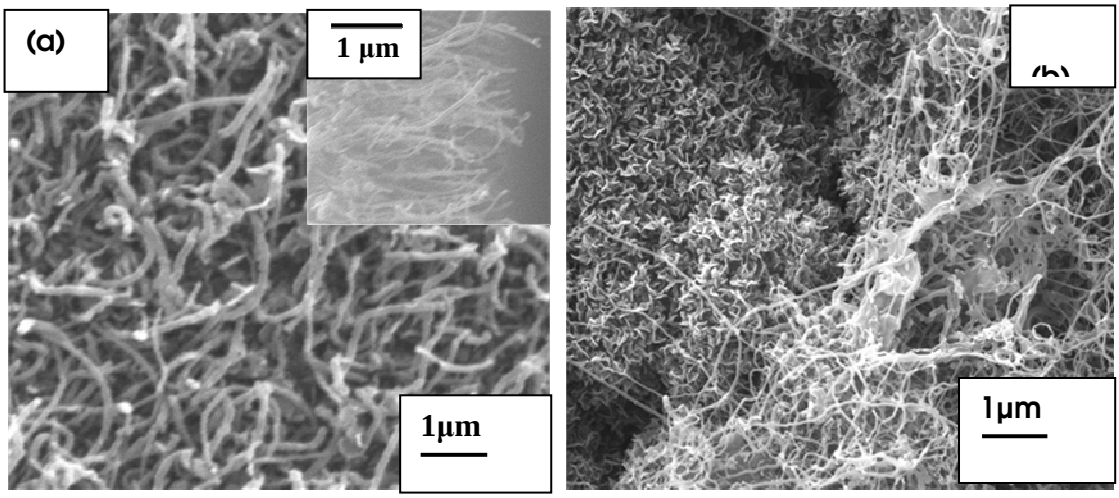

Fig.3.16: SEM micrograph of Ag with Fe catalyst (a) Ag film thickness of ~6 nm (b) film thickness of ~10 nm.

3.3 Summary

The structured parameters of various nanstructured carbon films synthesized have been summarized in Table 3.5. Samples having Ag underlayer, the length of CNT formed have been found to be maximum in sample A101 and without Ag underlayer the length of CNT is for maximum for sample F101 and thus the optimum thickness of Ag metal underlayer for the growth of CNTs having high aspect ratios. Thus using an metal underlayer we found long CNT as campared to without any underlayer, under the same conditions.

Table 3.5 Details of prepared samples.

Sample	Microstructure	I.D(nm)	O.D.(nm)	CNT length
A101	Dense CNTs	6-17	19-39	600-1.7 um
A102	Highly dense CNTs	4-21	18-31	500- 800nm
A103	flakes	-	-	-
F101	Less CNTs	6-12	13-38	300-500 nm
F102	Some CNTs with flakes	7-19	18-28 nm	250-450 nm
F103	flakes	-	-	-

CHAPTER 4

Field Emission Properties of Carbon nanostructures

This chapter contains introduction of field emission and measurements of different CNT films and nanowalls. A simple diode configuration was used for the field emission measurement in which cathode was made of a flat stainless steel plate on which carbon film on Si substrate were mounted. A highly polished stainless steel plate was used as anode. The field emission characteristics of different films have been correlated with their microstructural features.

4.1 Introduction

Field emission is a mechanism to extract electrons from a solid surface. It is a quantum effect where under a sufficiently high external electric field, electrons near the Fermi level tunnels through the energy barrier and escape to the vacuum level [65] (Fig.4.1) . Compared to thermionic emission, this is a preferred mechanism for certain applications because no heating is required and the emission current is almost solely controlled by the external field. The emission current from a metal surface is determined by the Fowler–Nordheim (F–N) equation:

$$I = aV^2 \exp(-b\varphi^{3/2}/\beta V)$$

Where I, V, φ, β are the emission current, applied voltage, work function, and field enhancement factor, respectively. For metal, with typical work function and a flat surface the threshold field is typically around 10^4 V/ μm which is impractically high. The work function is a basic material property that cannot be varied significantly.

All the field emission sources rely on field enhancement due to sharp tips/protrusions, so they tend to have smaller virtual source sizes because of the primary role of the β factor. The larger the β, the higher the field concentration, and therefore the lower the effective threshold voltage for emission.

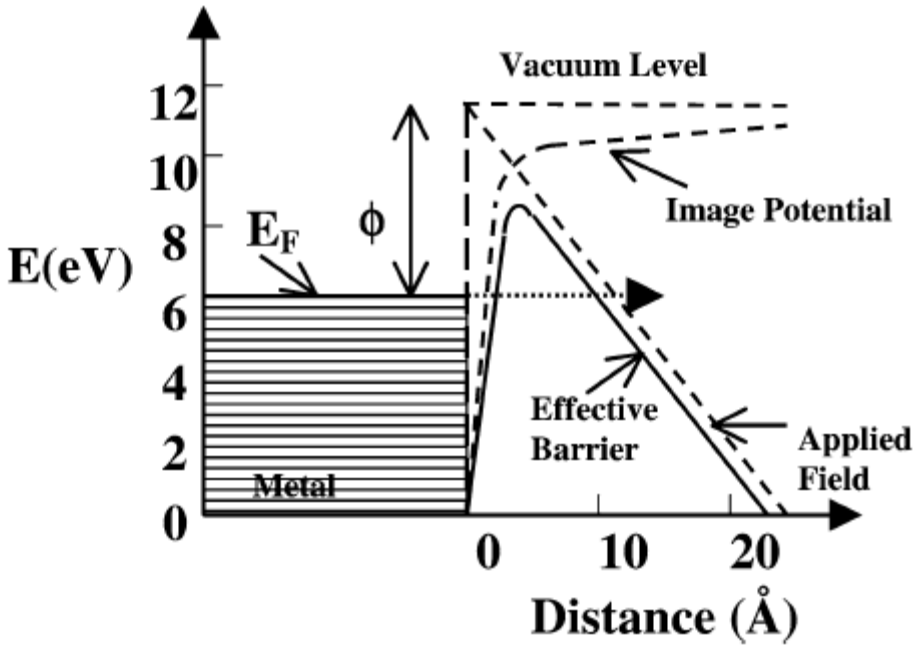

Fig.4.1: Potential- energy diagram shows the effect of an external electric field on the energy barrier for electrons at a metal surface.

A carbon nanotube (CNT) is a new carbon allotrope that was discovered in 1991[66]. Electron field emission from CNTs was first demonstrated in 1995 [67,68], and has since been studied extensively. CNTs have the right combination of properties: nanometer-size diameter, structural integrity, high electrical and thermal conductivity, and chemical stability [69], which makes them excellent electron emitters. Carbon nanotubes (CNT) have recently emerged as a promising class of electron field emitters. They have a low threshold electric field for emission and a high emission current density which make them attractive for technological applications.

In the first report of electron emission from CNTs, Rinzler et al. studied field emission from an individual multiwalled nanotube (MWNT) attached to a graphite fiber along the field direction [67]. With a bias voltage of less than 80 volts, emission currents of 0.1

to 1 μA were obtained at room temperature. They also reported that emission could be enhanced by opening the tips of the nanotubes. Density-functional theory calculations showed that under emission conditions large electric field present at the tube tip could stabilize the adsorbates and lower the ionization potential, thereby making it easier to extract electrons.

The CNTs can emit very large electron current. Experiments from a single MWNT tip revealed that it is capable of emitting stably for more than 100 hours at - 2 μA current [70]. Under the applied electric field, the CNTs can align along the field direction due to the electrostatic force [71]. SWNTs generally have a smaller diameter and higher degree of structural perfection than MWNTs hence a capability for achieving higher current densities and a longer life time . A theoretical study predicted that an open-ended SWNT has much better field-emission properties than a closed SWNT, due to the electronic effects that alter the bonding mode and decrease the work function. Individual CNTs are excellent electron field emitters with a low turn-on field for emission and a high emission current density. These emission characteristics are directly related to the unique structure and chemical bonding of the CNTs.

FE from CNTs has shown to be one of the most promising properties as far as its practical application is concerned. This is because CNTs present many advantages over conventional emitters due to their unique structure and properties such as (i) high chemical stability and high mechanical strength (ii) high melting point and reasonable conductivity (iii) high aspect ratios (iv) large- scale production at low cost, have longer life time and are capable of producing high current densities at low operating voltages [72].

4.2 Experimental set-up for field-emission studies

Field emission set-up (shown in Fig. 4.2) consists of a highly polished stainless steel UHV chamber having

(a) External diameter ~ 34 cm (b) Internal diameter ~ 29 cm (c) Height ~ 23.5 cm

The chamber has ports for fitting gauges for measuring low and high vacuum. Additional ports for feed-throughs for making electrical connections and a viewing window for monitoring are also present. Inside the chamber, there is arrangement for having the cathode and anode plate insulated from each other. The anode is a highly polished stainless

steel plate having a diameter of 19 cm. The movement of the cathode can be digitally controlled by using a controller to the accuracy of 5 μm, which in turn gives the adjustable distance between the cathode and anode. The chamber is connected to a rotary pump (DS 102 of Varian make) for obtaining initial vacuum of the order of 10^{-3} torr. The pressure upto this range is measured by digital Pirani gauge (model no PHG-11 of Vactech). A turbo pump (TV-301 Navigator of Varian) with turbo controller (Turbo- V 301 of Varian) is connected to the chamber through a separate port, with the help of which a vaccum of the order of 2×10^{-6} can be obtained. Pressure of this order can be measured with the help of a Penning gauge.

Fig.4.2: Experimental set-up for field emission studies.

The sample can be mounted on the cathode plate with silver paste. The anode plate is connected to the positive terminal of the high voltage DC power supply unit (model no H5K02N of Aplab of 5 k V rating) through an ammeter. A high resistance of 7.7 MΩ is connected in series with the power supply for limiting the current and to avoid accidental damage of power supply and current meter. The cathode is grounded to the power supply and also grounded to earth through the chamber body and mount. Schematic of the diode type field-emission measurement set-up is shown in Fig. 4.3.

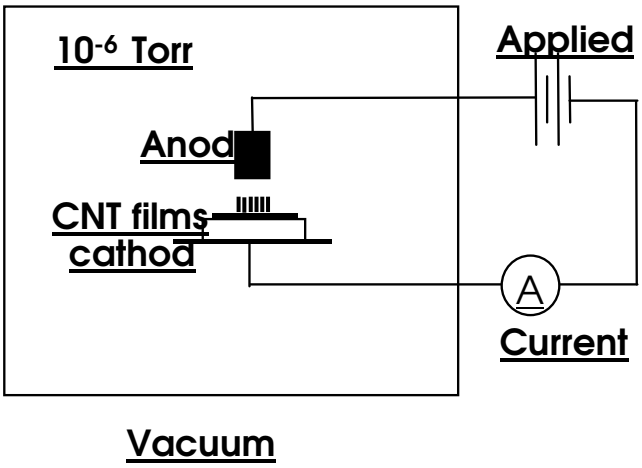

Fig.4.3: **Schematic of the diode type field-emission measurement set-up.**

A high resolution CMOS camera (ARTCAM-200MI) is assembled on top of the glass view port and interfaced with PC with high speed transfer via USB 2.0 interface for taking the in-situ pictures of emission from CNT films. For the I-V characteristic measurement, a circular polished SS plate was kept on the anode for collecting the electrons. While for emission pattern images, a conducting fluorescent screen is placed over the anode.

This field emission set-up has several salient features as listed below:

1. The chamber is of highly polished stainless steel material which makes the chamber UHV compatible.
2. A turbo molecular pump backed by a rotary pump is used to achieve a pressure of ~10^{-6} torr.
3. In situ adjustment of distance between the electrodes is possible without stopping the experiment.
4. Field emission images can be captured by the high precision CMOS camera and saved in PC in situ via the USB 2.0 interface.

The field emission measurement of nanostructured carbon films were carried out in a high vaccum chamber using a simple diode configuration. The schematic diagram of field emission measurement set up is shown in fig.4.2.

Field emission data was analyzed using Fowler – Nordheim (F-N) theory, according to which current density of a metal tip is dependent on the local electric field (E_{loc}) and chemical state(i.e. work function φ) of the emitter as

$$J \alpha \ (E^2_{loc} / \varphi) \exp (-B\varphi^{3/2}/E_{loc})$$

where $B = 6.83 \times 10^{9} \ VeV^{-3/2}m^{-1}$ The schematic of electron emission methodology from an emitter under the applied electric field and relation between the E_{loc} and the E and corresponding F-N formula are shown in fig 4.4.

In case of CNTs the value of β can be determined experimentally from the slope of F-N plot between In (I/V^2) versus 1/V provided φ is known. The slope of F- N plot is given by

$$\text{Slope} = - B \varphi^{3/2} d/ \beta$$

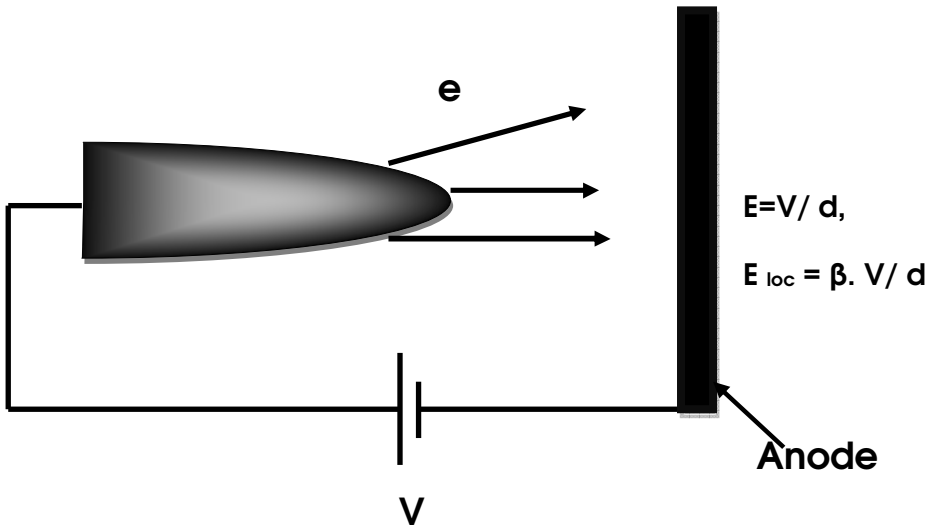

Fig.4.4: FE from a tip of nanotube.

4.3 Results and Discussion

4.3.1 Field Emission Characteristics of sample F101 and A101

Fig 4.4 (a) shows the J versus E plots of sample F101 and A101. The field emission quality of a sample is determined in terms of threshold field. The threshold field E_{th} (corresponding to 100μA/cm^2 emission current density) 3.8 V/μm was observed for F101 sample while for sample A101 it was 2.6 V/μm.

Field emission was found high β values and low threshold field for the sample A101 as campared to the F101 sample. This is due to increase in the density of CNT (due to which emitter site density increases) as discussed in chapter 3. It is suggested that presence of metal Ag underlayer provides low metal-CNT contact resistance[73] which leads to high emission current.

Fig.4.4 (b) shows the F-N plot of sample F101 and A101. For sample F101 deviation in the high field region F-N plot may be due to presence of defects which are not present in A101. Field enhancement factor are shown in table 4.1.

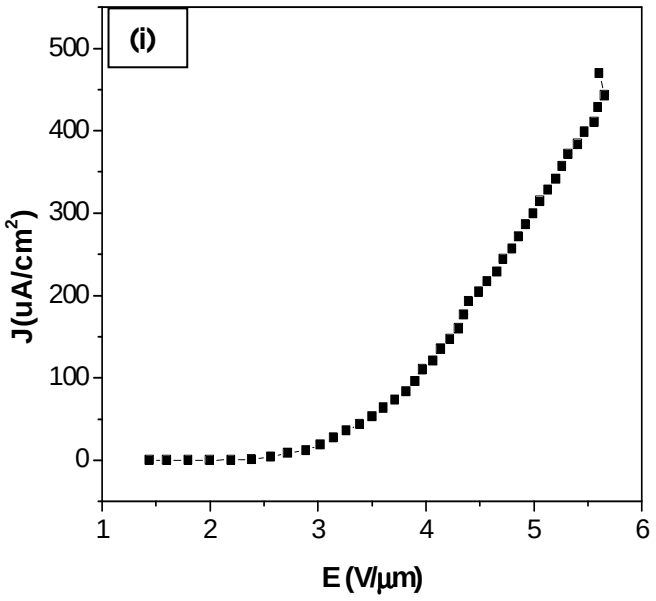

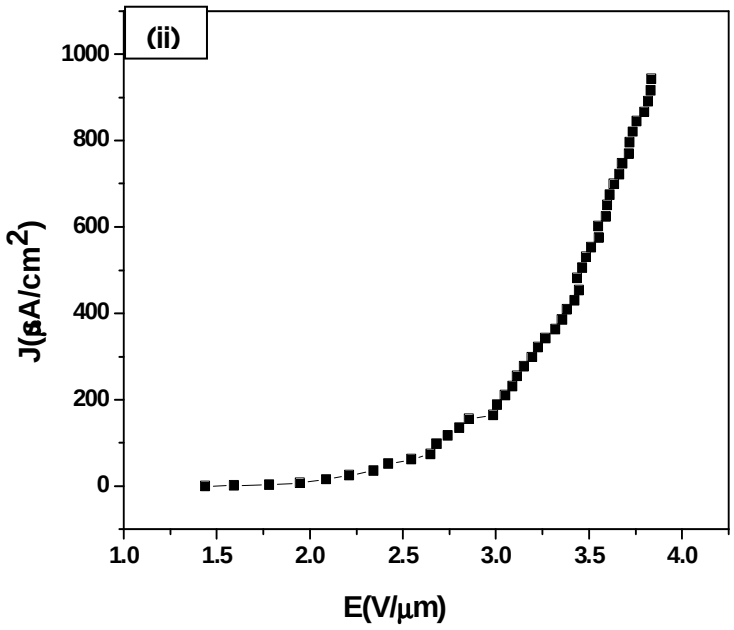

Fig.4.5(a): Emission Current density(J) vs. macroscopic field(E) (i) for sample F101 (ii)A101

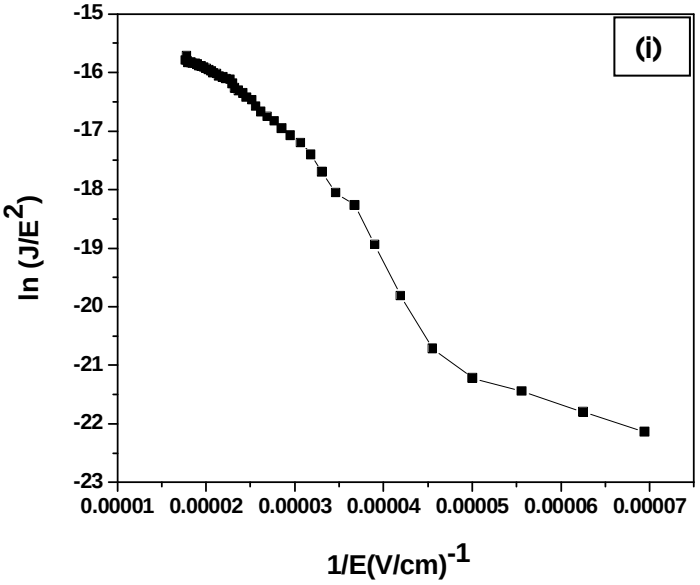

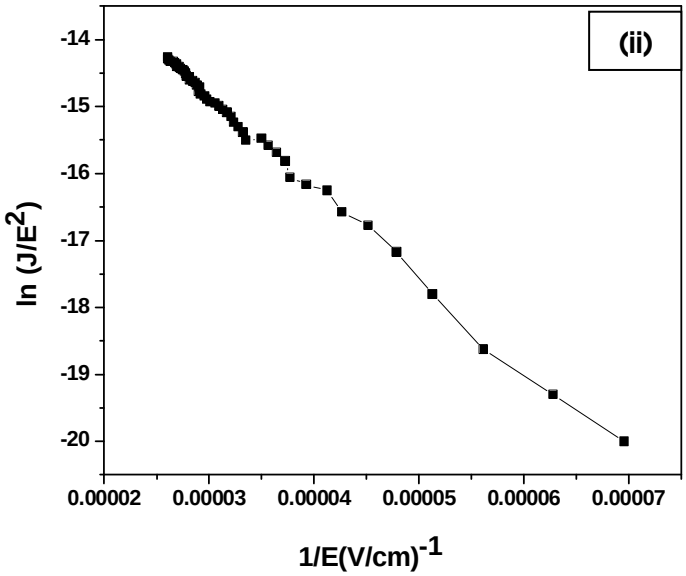

Fig.4.5(b): F-N plot for the samples (i) F101 (ii) A101

Table 4.1 FE Parameters for Carbon Nanotubes

Sample	**Threshold Field (V/μm)**	**Field Enhancement Factor(β)**
F101	3.8	2728
A101	2.6	4863

4.3.3 Field Emission Characteristics of Carbon Nanowalls (CNW)

Figure 4.5(a) shows current density (J) versus electric current (E) plots of sample A01 and A04. The best emission characteristic was observed in sample A04. The observed threshold field Eth values for these samples are given in table 4.1 it shows that the Eth value is less for sample A01 at less deposition time. The increased density, smaller size and improved alignment of CNW are possibly responsible for the decreased Eth values for samples with less deposition time. But the field enhancement factor is lager in case of A04 this may be due to the field amplification because the length is increased with increasing deposition time.

The corresponding F-N plots for all these two samples are given in fig.4.5(b). The straight line with negative slope in high field region clearly shows that the emission process from the CNW are also followed the F-N model. It is clear that sample A04 shows superior emission characteristics because of increased surface area of the CNW at higher growth time.

Table 4.2 FE Parameters for CarbonNanowalls.

Sample	**Threshold Field (V/μm)**	**Field Enhancement Factor(β)**
Ag01	4.3	2651
Ag04	4.4	4627

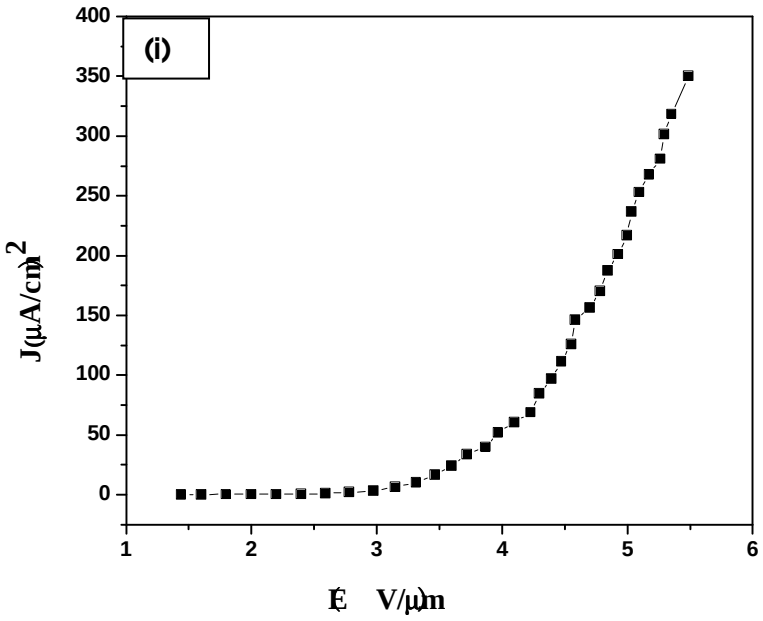

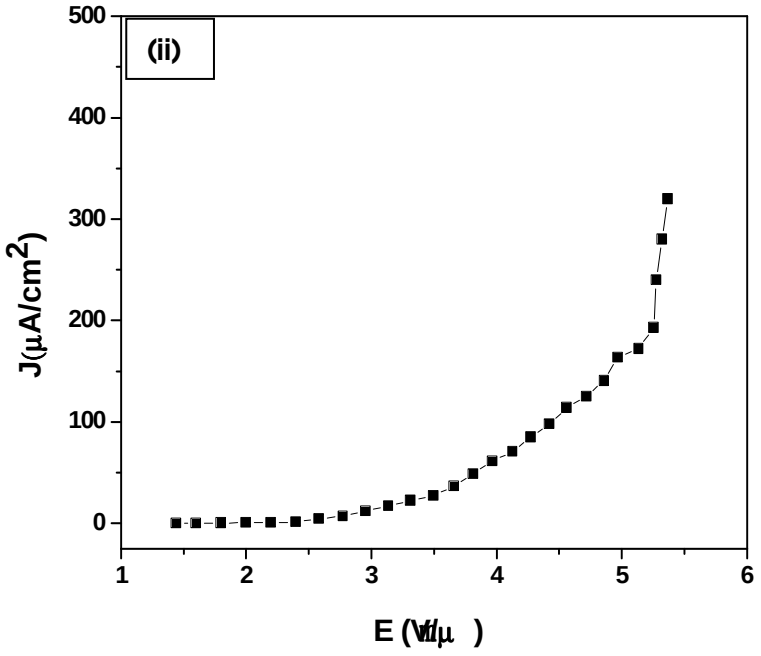

Fig.4.6(a): Emission Current density vs. macroscopic field (i) Ag01 (ii) Ag04

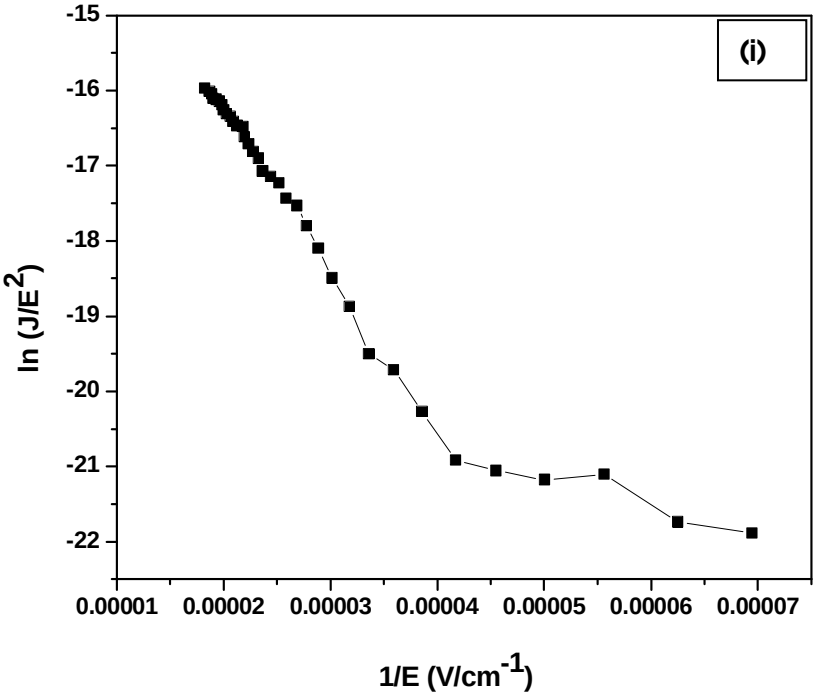

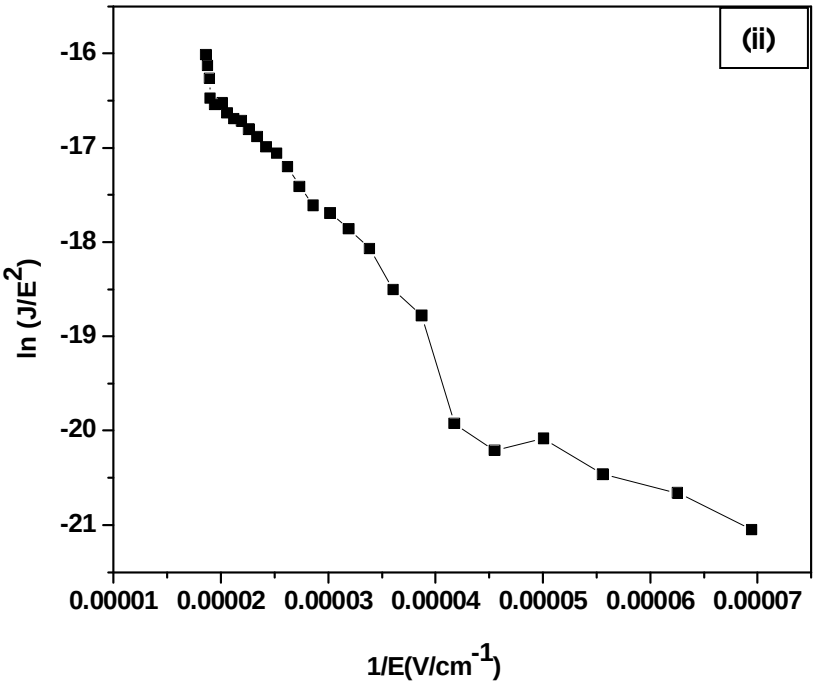

Fig.4.6(b): F-N plot for the samples (i) Ag01 (ii) Ag04

4.4 Summary

In our study it was found that, sample A101 (grown with Ag metal underlayer with Fe Catalyst layer) has low threshold field (2.6 V/μm) as campared to sample F101(3.8 V/μm) (grown on catalyst Fe layer). The value of β (4863) is also maximum for this sample (A101). The microstructure of this sample consisted of dense CNTs. Thus an Ag metal underlayer (~6 nm thick) has been observed to improve the field emission properties of CNT film.

Field emission by carbon nanowalls were also found good. The low threshold field of (4.3 V/μm) was found for sample A01 due to high density of nanowalls of smaller size. The field enhancement factor is found maximum for sample A04 (4627) due to increase the surface area of carbon nanowalls with increase in deposition time which increases the emission properties.

Conclusion

This work has been carried out to study the various growth related aspects of carbon nanostructures by MPECVD process and to correlate the microstructural features of the films to their field emission characteristics.

- The presence of Ag metal film (~ 6 nm thick) beneath the catalyst film increased the particle size distribution. GAXRD study of the pre-treated substrates confirmed the absence of Fe-Ag alloys.
- A comparative study was carried out for Ag-Fe and Fe films deposited on Si substrates. Highly dense and vertically aligned bamboo shaped CNTs were grown at gas flow ratio (C_2H_2:H_2)15:75 with deposition time 1 minute for all the samples. This infers that 1 minute was the optimum time for deposition to avoid formation of carbon nanoflakes over 1D structure. It was found that Ag-Fe film deposited on Si substrate provided better growth of CNTs as compared to the Fe films for the same growth parameters used. This was due to the increased particle size distribution. The structural parameters (length, diameter) of CNTs in the Ag-Fe film were found to be different than in the Fe film due to the presence of metal underlayer.
- The field emission measurements of different CNTs and CNWs were carried out in a diode configurated field emission system. The field emission study of CNTs and CNWs indicated that the electron emission process is dependent on the structure and surface morphology of the film. CNWs also showed good emission characteristics.
- In our study, the film consisting of CNTs grown over the substrate having Ag metal underlayer was observed to have low threshold field (~ 2.6V/μm) as compared to CNTs grown over Fe (~3.8V/μm). This has been attributed to the efficient electron emission from CNTs having high density. The presence of defects was also expected to enhance electron emission as open ends of graphite layers act as additional emission sites.
- CNWs also have good emission characteristics. On increasing the deposition time the CNWs were found to be good emitters having field enhancement factor 4627 which is due to the increase in the surface area with increase in the time of deposition.

Scope of future work

Mechanical and electronic properties of CNTs are expected to vary with variation in the alignment of CNTs.

- In the present study a metal underlayer was used to improve the structural properties hence further study on the growth mechanism of CNTs can be carried out to improve the alignment of CNTs, which can be useful in field electron transistors, Single electron transistors and rectifying diodes.
- CNTs can be patterned and aligned for fabricating functional devices such as: field emitters, scanning probe, sensors and nanoelectronics.
- The effect of different metal underlayers (Ti, Al) on the structure and field emission properties of CNT film can be carried out.
- Varying thickness of Ag metal underlayer can be further studied and investigation of field emission performance of different CNT and CNW with Ag as an underlayer may be carried out.

References

1. S. Iijima, Nature 354 (1991) 56.
2. L.X. Zheng et al. , Nature materials 3 (2004) 673-676.
3. R. Martel, V. Derycke, C. Lavoie, J. Appenzeller, K.K. Chen, J. Tersoff, Phy. Rev. Lett. 87 (2001) 256805.
4. J. Mannik, B.R. GoldSmith, A. Kane, P.G. Collins, Phys. Rev. Letts. 97 (2006) 016601.
5. S. M. Lee, K. H. An, Y. H. Lee, G. Seifert, and T. Frauenheim, J. Ame. Chemi. S.123 (2001) 5059.
6. P.J.F. Harris, Carbon nanotubes and Related Structures (Cambridge University Press UK) 1999.
7. J.W.G. Wildoer, L.C. Venema, A.G. Rinzler, R.E. Smalley and Dekker, Nature 391 (1998) 59.
8. T. W. Odom, J. L. Huang, P. Kim, C. M. Lieber, Nature 391 (1998) 62.
9. J. Han, in: M. Meyyappan (Ed.), Carbon Nanotubes Science and Applications, CRC press, Boca Ratton (2005) 1.
10. Hong, Seunghun; Sung Myung, Nature Nanotechnology 2 (2007) 207-208.
11. J. Hone, Dekker Encyclopedia of Nanoscience and Nanotechnology (2004) DOI: 10.1081/E-ENN 120009128, 603
12. M.M.J. Treacy, T.W. Ebbesen, J.M. Gibson, Nature 318 (1996) 678-680.
13. A. Krishnan, E. Dujardin, T. W. Ebbesen, P.N. Yianilos, M.M.J. Treacy, Phys. Rev. B 58 (1998), 14013-14019.

14. S. C. Lim, H. J. Jeong, K.H. an, D. J. Bae, Y. H. Lee, Y.M.Shin, Y. C. Choi, in: H.S. Nalwa (Ed.), Encyclopedia of Nanoscience and Nanotechnology, vol. 1, American Scientific Publishers (2004) 611.
15. B. Q. Wei et al., Appl. Phys. Lett. 79 (2001) 1172.
16. N. De Jonge, Y. Lamy, K. Schoots, T. H. Oosterkamp, Nature 420 (2002) 393.
17. B. Gao, Chem. Phys. Lett. 327 (2000) 69.
18. R. Z. Ma et al., Science in China Series E-Technological Sciences 43 (2000) 178.
19. D. Walters et al., Chem. Phys. Lett. 338 (2001) 14.
20. Y. Ando, Jpn. J. Appl. Phys. 32 (1993) L1342.
21. Y. Saito et al., Chem. Phys. Lett. 200 (1992) 643.
22. Y. Ando and S. Iijima, Jpn. J. Appl. Phys. 32 (1993) L107.
23. T. W. Ebbesen and P. M. Ajayan, Nature 358 (1992) 220.
24. D. T. Colbert et al., Science 266 (1994) 1218.
25. S. Iijima and T. Ichihashi, Nature 363 (1993) 603.
26. D. S. Bethune et al., Nature 363 (1993) 605.
27. X. Zhao et al., Carbon 35 (1997) 775.
28. Y. Ando et al., Carbon 35 (1997) 153.
29. H.W. Kroto, J.R. Heath, S.C. O'Brien, R.F. Curl and R.E. Smalley, Nature 318 (1985) 162.
30. T. Guo, P. Nikolaev, A.G. Rinzler, D. Tomanek, D.T. Colbert and R.E. Smalley, J. Phys. Chem. 99 (1995) 10694.
31. T. Guo, P. Nikolaev, A. Thess, D.T. Colbert and R.E. Smalley: Chem. Phys. Lett. 243 (1995) 49.
32. J. B. Park et al., Journal of Crystal Growth 244 (2002) 211-217.

33. Milton Ohring, Materials science of thin films, Stevens Institute of technology, Hoboken, New jersey.

34. M. Chen, M. M. Chen and C.F. Chen, Journal of Materials Science, 37 (2002) 3561-3567.

35. L. Valentini, J. M. Kenny, L. Lozzi and S. Santucci J. Appl. Phys. 92 (2002) 6188.

36. A.D. Macdonald, Microwave Breakdown in gases, John Wiley and sons, Inc., New York, 1996, p.3,5.

37. P. Leprince, J. Marec, M. Capitelli and C. Gorse (Eds.), Plasma Technology: Fundamentals and Applications, Plenum Press, New York (1992) 167.

38. H. C. Barshilia, B.R. Mehta and V.D. Vankar, J. Mater. Res. 11 (1997) 1019.

39. G. Kamalakar, D. W. Hwang and L. Pin. Hwang, J. Mater. Chem. 12 (2002) 1819.

40. Y. Saito-and S. Uemura, Carbon 38 (2000) 169.

41. T. W. Odom, J. L. Huang, P. Kim and C. M. Lieber - Nature, 1998 - leitl.org

42. P. J. Harris, Carbon nanotubes and related structures, Department of chemistry, Cambridge University press.

43. WWW.physorg.com.

44. Y. Ando, X. Zhao, T. Sugai, and M./ Kumar, Materials Today 7 (2004) 24-29.

45. C. Journet, P. Bernier, Applied Physics A, Materials Science & Processing, Springer-Verlag 1998.

46. M.Dainen, R.D. de Fouw (ST), B.Hamers (ST, Treasurer), P.G.A. Janssen (ST) and K. Schouteden(N). The Woundrous World of carbon nanotubes (2003).

47. P. J. Grundy and G. A. Jones, Electron Microscopy in the study of Materials, Edward Arnold Ltd., London, 1976.

48. J. Goldstein, Dale E. Newbury, D. C. Joy, Charles E. Lyman and P. Echlin, Scanning Electron Microscopy and X- ray Microanalysis, Springer, 2003-02.

49. R. Andrews, D. Jacques, A.M. Rao, F. Derbyshire, D. Qian, X. Fan and E.C. Dickey, J. Phys. Chem. B 101 (1997) 8839.

50. David B. Williams and C. Barry carter, Transmission Electron Microscope, Springer 2004-08-31.

51. D. B. Williams and C.B. Carter, Transmission Electron Microscopy, Basics I, Plenum Press, New York, 1996.

52. D. B. Williams and C.B. Carter, Transmission Electron Microscopy, Imaging III, Plenum Press, New York, 1996.

53. Gardiner, D.J. (1989). Practical Raman spectroscopy. Springer-Verlag. ISBN 978-0387502540.

54. A. M. Bonnot, Phys. Rev. B 41 (1990) 6040.

55. U. P. Agarwal, R. H. Atalla and J. S. Bond, Springer- Verlag berlin Heidelberg (1992) 162.

56. A. Thess, R. Lee, P. Nikolaev, H. Dai, P. Petit, J. Robert, C. Xu, Y.H.Lee, S.G. Kim, A. G. Rinzler, D.T. Colbert, G.E. Scuseria, D. Tomanek, J.E. Fischer and R.E. Smalley, Science 273 (1996) 483.

57. P.W. Flynn, in: D.M. Considine (Ed.) Scientific Encyclopedia, 7^{th} ed., vol.2, van Nostrand's Publication, New York (1989) p. 2088.

58. B. D. Cullity, Elements of X- ray Diffraction, Addision-Wisley, MA,1978.

59. B. Wang, X. Liu, H. Liu, D. Wu and H. Wang, Materials Chemistry, Donghua University, Shanghai 200051, china.

60. H. Kanzow and A. Ding, Phys. Rev. B 60 (1999) 11180.

61. C. H. Lin, H.L. Chang, M.H. Tsai and C.T. Kuo, Diamond Relat. Mater. 11 (2002) 922.

62. C. Bower, W. Zhu, S. Jin and O. Zhou, Appl. Phys. Lett. 77 (2000) 830.

63. S. Kurita, A. Yoshimura, H. Kawamoto, T. Uchida, K. Kojima, M. Tachibana et al. , J Appl phys 2005;97: 104320-5.

64. Ni ZH, Fan HM, Feng YP, Shen ZX, Yang BJ and Wu YH. Raman spectroscopic investigation of carbon nanowalls. J Chem Phys 124 (2006) 204703-5.

65. R. Gomer, Field Emission and Field Ionization, Harvard University Press, Cambridge, MA, 1961

66. S. Iijima, Helical microtubules of graphitic carbon, Nature 354 (1991) 56–58.

67. A.G. Rinzler, J.H. Hafner, P. Nikolaev, L. Lou, S.G. Kim, D. Tomanek, D. Colbert and R.E. Smalley, Science 269 (1995) 1550–1553

68. W.A.D. Heer, A. Chatelain and D. Ugarte, Science 270 (1995) 1179–1180.

69. M.S. Dresselhaus, G. Dresselhaus and P. Avouris (Eds.), Appl. Phys., Vol. 80, Springer-Verlag, Heidelberg, 2000.

70. J.M. Bonard, F. Maier, T. Stökli, A. Chäelain, W.A. de Heer, J.-P. Salvetat and L. Forr, Ultramicroscopy 73 (7) (1998).

71. Z.L. Wang, R.P. Gao, W.A.D. Heer and P. Poncharal, Appl. Phys. Lett. 80 (5) (2002) 856–858.

72. Z. P. Huang, Y. Tu, D. L. Carnahan and Z. F. Ren, in: H. S. Nalwa (Ed.), Encyclopedia of Nanoscience and Nanotechnology, vol. 3, American Scientific Publishers, 2004, p. 401

73. P. M. Parthangal, R. E. Cavicchi and Michael R. Zachariah, National Institute of Standards and Technology, Gaithersburg, MD 20899, USA.